

Simulating galactic outflows with thermal supernova feedback

Claudio Dalla Vecchia^{1,2*} and Joop Schaye^{2†}

¹*Max Planck Institute for Extraterrestrial Physics, Giesenbachstraße 1, 85748 Garching, Germany*

²*Leiden Observatory, Leiden University, P.O. Box 9513, 2300 RA Leiden, the Netherlands*

10 July 2018

ABSTRACT

Cosmological simulations make use of sub-grid recipes for the implementation of galactic winds driven by massive stars because direct injection of supernova energy in thermal form leads to strong radiative losses, rendering the feedback inefficient. We argue that the main cause of the catastrophic cooling is a mismatch between the mass of the gas in which the energy is injected and the mass of the parent stellar population. Because too much mass is heated, the temperatures are too low and the cooling times too short. We use analytic arguments to estimate, as a function of the gas density and the numerical resolution, the minimum heating temperature that is required for the injected thermal energy to be efficiently converted into kinetic energy. We then propose and test a stochastic implementation of thermal feedback that uses this minimum temperature increase as an input parameter and that can be employed in both particle- and grid-based codes. We use smoothed particle hydrodynamics simulations to test the method on models of isolated disc galaxies in dark matter haloes with total mass 10^{10} and $10^{12}h^{-1} M_{\odot}$. The thermal feedback strongly suppresses the star formation rate and can drive massive, large-scale outflows without the need to turn off radiative cooling temporarily. In accord with expectations derived from analytic arguments, for sufficiently high resolution the results become insensitive to the imposed temperature jump and also agree with high-resolution simulations employing kinetic feedback.

Key words: methods: numerical — ISM: bubbles — ISM: jets and outflows — galaxies: evolution — galaxies: formation — galaxies: ISM

1 INTRODUCTION

It is widely accepted that star formation (SF) feeds back energy into the interstellar medium (ISM). The energy released by massive stars, both through stellar winds and core-collapse supernova (SN) explosions, can efficiently suppress SF by evaporating dense, star-forming clouds, by generating supersonic turbulence and, eventually, by generating powerful, large-scale outflows that eject gas from galaxies and enrich the intergalactic medium.

Modern cosmological simulations that follow the formation and evolution of galaxies still lack both the resolution and the physics that is required to model the multi-phase ISM and individual massive stars or SN explosions. The same is true for simulations of individual galaxies, although the resolution of such models is now sufficient to begin to crudely disentangle the relative roles of the differ-

ent mechanisms through which massive stars inject energy and momentum (e.g. radiation pressure vs. SN explosions, Hopkins, Quataert, & Murray 2012). Thus, in naive implementations of stellar feedback, “star” particles representing simple stellar populations (SSPs) distribute “SN energy” over neighbouring resolution elements at each time step. This procedure is well-known to be inefficient, in that most of the thermal energy is radiated away before it can be converted to kinetic energy (e.g. Katz, Weinberg, & Hernquist 1996).

Three types of sub-grid recipes are commonly used to solve the over-cooling problem: injecting the energy in kinetic form (e.g. Navarro & White 1993; Mihos & Hernquist 1994; Kawata 2001; Kay et al. 2002; Springel & Hernquist 2003; Oppenheimer & Davé 2006; Dalla Vecchia & Schaye 2008; Dubois & Teyssier 2008; Hopkins, Quataert, & Murray 2012), suppressing radiative cooling by hand (e.g. Gerritsen 1997; Mori et al. 1997; Thacker & Couchman 2000; Kay et al. 2002; Sommer-Larsen, Götz, & Portinari 2003; Brook et al.

* E-mail: caius@mpe.mpg.de

† E-mail: schaye@strw.leidenuniv.nl

2004; Stinson et al. 2006; Piontek & Steinmetz 2011), and decoupling the different thermal phases by hand (e.g. Marri & White 2003; Scannapieco et al. 2006; Murante et al. 2010). Each solution has its own pros and cons and all require the specification of sub-grid parameters. The different approaches should converge when the resolution is increased, although it is not obvious that this will in fact happen.

The inefficiency of thermal feedback is usually attributed to a lack of resolution: the energy is deposited in gas that is too dense, because the hot, low-density, bubbles that fill much of the volume of the multiphase ISM are missing. However, as we pointed out in Dalla Vecchia & Schaye (2008, hereafter DS08), a more fundamental problem is the fact that the SN energy is distributed over too much mass, which implies that the temperature of the SN heated gas is too low and hence the cooling time too short. Indeed, in reality one SNII is produced for every $\sim 10^2 M_\odot$ of stars, and the energy released in the explosion is initially carried by $\ll 10^2 M_\odot$ of ejecta. Hence, the ratio of the mass of the ejecta and the mass of the stellar population that released the energy is small $\ll 1$. In contrast, in simulations this ratio is $\gg 1$, unless the mass of star particles is very large compared with that of the surrounding gas resolution elements, which is typically not the case. Increasing the resolution does not change the ratio between the mass of a star particle and the mass of the neighbouring resolution elements (although it may in the case of grid simulations) and hence is unlikely to solve the over-cooling problem by itself.

The temperature jump of the gas receiving feedback energy can be increased by storing the energy until it suffices to heat the gas by a desired amount. Indeed, this strategy is for example used in some sub-grid recipes for feedback from active galactic nuclei (AGN), which store the AGN energy in the black hole until the neighbouring gas can be heated to a desired temperature (Booth & Schaye 2009). This approach is, however, not suitable for SN feedback. Storing the energy in a star particle would not help because standard implementations of thermal SN feedback are inefficient even if all the SN energy of an SSP is released at once. Storing energy in gas particles is undesirable because it would make the feedback non-local, which would for example mean that heavy elements released by the star particle are less likely to be carried by outflows.

An alternative way to increase the temperature jump is to reduce the ratio of the heated mass to the mass of a star particle. This can be done by reducing the number of neighbouring resolution elements that are heated, but that does not help if even a single resolution element contains too much mass. Moreover, this approach would result in a range of temperatures if not all resolution elements have the same mass. To guarantee the efficiency of the feedback, one would like to be able to specify the temperature jump of the gas that receives energy. This can be accomplished by making the thermal feedback stochastic: the probability that a neighbouring resolution element is heated will then depend on the desired temperature jump and on the ratio of the mass of the star particle to that of the neighbouring gas resolution element.

A stochastic approach to thermal feedback was tried, and found to be effective, by Kay, Thomas, & Theuns (2003) in smoothed particle hydrodynamics (SPH) simula-

tions of groups of galaxies. For each simulation time-step and each star particle, they integrated the energy released by SNe and distributed it stochastically to its nearest gas neighbour. They only considered the limiting case in which the temperature jump was sufficiently high that the number of particles that could be heated per time step was less than one.

In this paper we generalise the method of Kay, Thomas, & Theuns (2003) to work also for temperature jumps sufficiently low for multiple neighbours to be heated. Using SPH simulations of isolated disc galaxies embedded in dark haloes with total mass 10^{10} and $10^{12} h^{-1} M_\odot$, we show that our implementation of thermal feedback is able to strongly suppress SF, to alter the morphology of the galaxy and to generate galactic winds. Reassuringly, for our high-resolution simulations we reproduce the results of DS08, where we simulated the same disc galaxies with kinetic feedback.

This paper is organised as follows. We compute the energy provided by core collapse SNe (SNII) in Section 2, where we show that for a standard initial mass function (IMF), a single star particle produces enough SN energy to heat a gaseous mass equal to the mass of the star particle by a few keV, a temperature that is sufficiently high for radiative cooling to be relatively inefficient. We present our numerical implementation for thermal SN feedback in SPH in Section 3, where we also compute some useful quantities as a function of the free parameters of the method: the amount of SN energy injected per unit stellar mass and the desired temperature jump. We also explain how the method could be adapted for grid simulations. We dedicate Section 4 to the derivation of the resolution constraints of our feedback recipe, which follow from the requirement that the radiative cooling time exceeds the sound crossing time across the heated resolution element so that the thermal energy is efficiently converted into kinetic form. After describing our simulations of isolated discs galaxies in Section 5, we present our results in Section 6. Finally, we summarise and discuss our conclusions in Section 7.

Videos and high-resolution images can be found at: <http://www.strw.leidenuniv.nl/DS12/>

2 ENERGY PROVIDED BY SNII

Each star particle is treated as a simple (or single) stellar population. Thus, its stellar content is simply described by an IMF, $\Phi(M)$. The number of stars per unit stellar mass ending their life as SNII, n_{SNII} , is then the integral of the IMF over the mass range $[M_0, M_1]$,

$$n_{\text{SNII}} = \int_{M_0}^{M_1} \Phi(M) dM, \quad (1)$$

where M_0 and M_1 are the minimum and maximum initial mass of stars that will explode as core collapse SNe. Throughout the paper we will use a Chabrier IMF and the mass interval $[M_0, M_1] = [6, 100] M_\odot$, although we also report calculations for a Salpeter IMF and for the widely used mass range of $[8, 100] M_\odot$ (6-8 M_\odot stars explode as electron capture SNe in models with convective overshoot; e.g. Chiosi, Bertelli, & Bressan 1992). For the Chabrier (Salpeter) IMF we obtain, for the mass range

$[M_0, M_1] = [6, 100] M_\odot$, $n_{\text{SNII}} = 1.736 \times 10^{-2} M_\odot^{-1}$ ($1.107 \times 10^{-2} M_\odot^{-1}$). For the mass range $[M_0, M_1] = [8, 100] M_\odot$, we have $n_{\text{SNII}} = 1.180 \times 10^{-2} M_\odot^{-1}$ ($0.742 \times 10^{-2} M_\odot^{-1}$).

The total available energy per unit stellar mass provided by SNII, $\epsilon_{\text{SNII}} = n_{\text{SNII}} E_{\text{SNII}}$, is given by

$$\epsilon_{\text{SNII}} = 8.73 \times 10^{15} \text{ erg g}^{-1} \left(\frac{n_{\text{SNII}}}{1.736 \times 10^{-2} M_\odot^{-1}} \right) E_{51}, \quad (2)$$

where $E_{\text{SNII}} \equiv E_{51} \times 10^{51} \text{ erg}$ is the available energy from a single SNII event and we will assume $E_{51} = 1$. The amount of energy from SNII available in a SSP particle is then $m_* \epsilon_{\text{SNII}}$, where m_* is the initial mass of the star particle.

If the energy is used to heat a gas mass $m_{\text{g,heat}}$, then the corresponding temperature increase is given by

$$\begin{aligned} \Delta T &= (\gamma - 1) \frac{\mu m_{\text{H}}}{k_{\text{B}}} \epsilon_{\text{SNII}} \frac{m_*}{m_{\text{g,heat}}} \\ &= 4.23 \times 10^7 \text{ K} \left(\frac{n_{\text{SNII}}}{1.736 \times 10^{-2} M_\odot^{-1}} \right) \left(\frac{\mu}{0.6} \right) \times \\ &\quad E_{51} \frac{m_*}{m_{\text{g,heat}}}, \end{aligned} \quad (3)$$

where $\gamma = 5/3$ is the ratio of specific heats for an ideal monatomic gas, k_{B} is the Boltzmann constant, m_{H} is the mass of the proton, and μm_{H} is the mean particle mass. We have assumed the gas to be monatomic and neglected the energy used to increase the degree of ionisation of the plasma.

The standard SPH approach is to distribute the SN energy over all neighbours of a star particle.¹ The heated mass is then $m_{\text{g,heat}} = N_{\text{ngb}} m_{\text{g}}$, where N_{ngb} is the number of neighbouring particles (typically 32–64, we use 48 in our simulations) and m_{g} is the mass of a single gas particle. Assuming $m_* = m_{\text{g}}$, we can see from equation (3), that the average temperature increase for the heated gas particles is $\sim 10^6 \text{ K}$, which falls in the temperature regime for which the cooling time is relatively short (e.g. Wiersma, Schaye, & Smith 2009a). Note that this procedure leads to even lower temperature increases if $m_* < m_{\text{g}}$, which happens if multiple star particles are produced by each star-forming gas particle. Heating only a single gas particle would give a temperature increase of $\sim 10^{7.5} \text{ K}$ and, as we will show, a much longer cooling time. As we will describe in the next section, we will make the temperature increase ΔT a free parameter and stochastically heat neighbouring gas particles.

3 THERMAL FEEDBACK IMPLEMENTATION

For simplicity and for consistency with DS08, we assume that all the SN energy produced within a star particle becomes available in a single time step. Once a stellar particle reaches an age $t_{\text{SN}} = 3 \times 10^7 \text{ yr}$, corresponding to the maximum lifetime of stars that end their lives as core collapse SNe, it stochastically injects thermal energy into its surroundings. Another reason why we prefer to impose this small time delay, is that it prevents the injection of energy

before the release of heavy elements by (the progenitors of) SNe, a process that happens continuously in our stellar evolution prescription (Wiersma et al. 2009b).

We note that it is straightforward to modify our implementation of thermal feedback to the case where SN energy is released stochastically over multiple time steps. All one needs to do, is to replace ϵ_{SNII} in the equations below by the energy per unit mass that is released by the star particle over the current time step. We tested this approach and did not find any significant difference.

Before providing a detailed description of our implementation of thermal SN feedback, we first describe the two free parameters used in our model.

3.1 Free parameters

Our recipe uses two free parameters. The first parameter, f_{th} , is the fraction of the available SN energy that is actually used in performing the feedback.² The value of f_{th} is between zero and unity, and can be used to control the efficiency of the feedback. Note that this parameter is not particular to our method, it is common to all implementations of SNII feedback.

We will present simulations that use either $f_{\text{th}} = 0.4$ or $f_{\text{th}} = 1$. The former value is used for comparison with the kinetic feedback of DS08, where we used the same value. It was also used by Schaye et al. (2010), who already showed some results of cosmological simulations that used the prescription for thermal feedback presented here. For most of our runs we will use $f_{\text{th}} = 1$ because it is an interesting limiting case and because high values can be justified for thermal feedback since we are in fact simulating radiative losses (we do not at any point turn off radiative cooling).

As discussed in the introduction, we wish to control the temperature increase of the heated gas particles in order to avoid the regime of short cooling times. We accomplish this by making the temperature increase ΔT , or rather the increase of the thermal energy per unit mass $\Delta \epsilon$, the second free parameter. Although $\Delta \epsilon$ is the parameter we actually use, we will often refer to the more intuitive corresponding value of ΔT , computed assuming the gas to be fully ionised ($\mu = 0.6$). Our fiducial temperature increase is $\Delta T = 10^{7.5} \text{ K}$, but we will explore a range of values.

Simulations employing the recipe described here should use values of ΔT sufficiently high to avoid catastrophic cooling. As shown analytically in section 4, the required minimum value will depend on the resolution. The remaining freedom, particularly the value of f_{th} , including possible dependencies on local physical conditions, can be used to calibrate the method by comparing the predictions for the quantities of interest to observations. Naturally, the best-fit parameter values may depend on other numerical and physical parameters.

¹ The standard approach is to weigh the contribution to each receiving gas particle by the SPH kernel. We ignore this weighting here for simplicity and because differences between SPH neighbours are by definition poorly resolved.

² We do not treat the energy per SN, E_{51} , as a free parameter because it is relatively well constrained by observations and because changes in E_{51} are in any case degenerate with changes in f_{th} .

3.2 Distributing the energy

In this section we derive the stochastic formulation for the energy injection. The energy released by a single star particle is shared among a fraction of the N_{ngb} neighbouring resolution elements. We will hereafter refer to resolution elements as “particles” but note that the same method will also work for grid simulations (replace “particle” by “cell”). We give each gas particle the same probability p of receiving energy from the star, irrespective of its mass (and, for the case of SPH, irrespective of its kernel weight). We draw a random number $0 \leq r \leq 1$ for each star-gas particle pair, and increase the internal energy of the gas particle by $\Delta\epsilon$ if $r \leq p$. We will now derive the value of the probability p .

The expectation value for the total amount of energy from SNII injected by a single star particle in the surrounding medium is

$$p \sum_{i=1}^{N_{\text{ngb}}} E_i = p \Delta\epsilon \sum_{i=1}^{N_{\text{ngb}}} m_i, \quad (4)$$

where E_i and m_i are, respectively, the total energy given to and the mass of gas particle i . We require the mean injected energy to equal the energy contributed by the star particle, $f_{\text{th}} m_* \epsilon_{\text{SNII}}$, from which the probability p follows:

$$p = f_{\text{th}} \frac{\epsilon_{\text{SNII}}}{\Delta\epsilon} \frac{m_*}{\sum_{i=1}^{N_{\text{ngb}}} m_i}. \quad (5)$$

Thus, the probability that a gas particle is heated is proportional to f_{th} , the fraction of total available SNII energy that the star particle shares with the surrounding gas, and inversely proportional to $\Delta\epsilon$, the amount of thermal energy per unit mass that is given to each heated gas particle.

The stochastic treatment breaks down if the probability is larger than one, because in that case the average amount of injected energy is lower than the required value. Imposing $p \leq 1$ puts a constraint on the value of the parameter $\Delta\epsilon$:

$$\Delta\epsilon \geq f_{\text{th}} \epsilon_{\text{SNII}} \frac{m_*}{\sum_{i=1}^{N_{\text{ngb}}} m_i} \simeq \frac{f_{\text{th}} \epsilon_{\text{SNII}}}{N_{\text{ngb}}}, \quad (6)$$

where the last equality holds exactly if all particles (gas and stars) have the same mass, as is usually approximately true for SPH simulations.

For a Chabrier IMF, assuming $N_{\text{ngb}} = 48$ and $f_{\text{th}} = 1$, we obtain $\Delta\epsilon \geq 1.82 \times 10^{14} \text{ erg g}^{-1}$, which corresponds to a temperature increase $\Delta T \geq 8.8 \times 10^5 \text{ K}$. For our fiducial choice for the temperature increase of $10^{7.5} \text{ K}$ we are well above this lower limit. For the case of grid simulations it is in principle possible that $\sum_{i=1}^{N_{\text{ngb}}} m_i \ll m_*$ and hence that $p > 1$. In that case it is necessary to increase $\Delta\epsilon$ above the chosen value in order to limit the probability to unity.

The sum of the probability over all neighbours gives the expectation value for the number of heated neighbours:

$$\langle N_{\text{heat}} \rangle = f_{\text{th}} \frac{\epsilon_{\text{SNII}}}{\Delta\epsilon} \frac{m_* N_{\text{ngb}}}{\sum_{i=1}^{N_{\text{ngb}}} m_i} \simeq \frac{f_{\text{th}} \epsilon_{\text{SNII}}}{\Delta\epsilon}, \quad (7)$$

where the last equality holds exactly if all particles have the same mass. The average number of heated neighbours is inversely proportional to $\Delta\epsilon$ and proportional to f_{th} . Expressed in terms of the temperature increase ΔT , the mean

number of heated neighbours is

$$\langle N_{\text{heat}} \rangle = 1.34 E_{51} \left(\frac{n_{\text{SNII}}}{1.736 \times 10^{-2} \text{ M}_{\odot}^{-1}} \right) \left(\frac{\mu}{0.6} \right) \times f_{\text{th}} \left(\frac{\Delta T}{10^{7.5} \text{ K}} \right)^{-1}. \quad (8)$$

Ideally, the energy should on average be shared with at least one gas neighbour to make the feedback local to the star particle and to ensure that the metals released by massive stars can be driven outwards. By injecting all the SNII energy from a SSP at once, we can satisfy this constraint for temperature increases that are sufficiently large to make radiative cooling (initially) inefficient.

4 ENSURING EFFECTIVE FEEDBACK: RESOLUTION REQUIREMENTS

The thermal feedback can only be effective if the heated gas responds hydrodynamically to the temperature increase before the thermal energy is radiated away. This implies that the sound-crossing time scale across a heated resolution element, t_s , must be short compared with the radiative cooling time scale in the heated gas, t_c . If this condition is satisfied, then the gas will start to expand adiabatically, doing work on its surroundings and converting thermal energy into kinetic energy. The ratio t_s/t_c can be decreased either by increasing t_c , which can usually be accomplished by increasing the temperature, or by decreasing t_s , which means increasing the temperature and/or the spatial resolution.

The sound crossing time across a resolution element of length h is

$$t_s = \frac{h}{c_s} = \left(\frac{\mu m_{\text{H}}}{\gamma k_{\text{B}}} \right)^{1/2} \frac{h}{T^{1/2}} \\ = 1.15 \times 10^5 \text{ yr} \left(\frac{\mu}{0.6} \right)^{1/2} \left(\frac{T}{10^{7.5} \text{ K}} \right)^{-1/2} \left(\frac{h}{100 \text{ pc}} \right), \quad (9)$$

where c_s is the local sound speed. This time scale is related to the classical definition of the Courant time step, $\Delta t = Ch/c_s = Ct_s$, where C (< 1) is the Courant factor.

We define the radiative cooling time as

$$t_c = \frac{u}{\Lambda} = \frac{\rho \epsilon}{\Lambda}, \quad (10)$$

where u and Λ are the internal energy and radiative cooling rate per unit volume, respectively, and ρ is the gas density. The internal energy per unit volume can be written as

$$u = \frac{1}{\gamma - 1} \frac{k_{\text{B}} T}{\mu m_{\text{H}}} \rho = \frac{1}{\gamma - 1} \frac{k_{\text{B}} T}{\mu X_{\text{H}}} n_{\text{H}}, \quad (11)$$

where n_{H} and X_{H} are the hydrogen number density and mass fraction, respectively. Before showing results for general cooling functions, we will consider the case of pure Bremsstrahlung, which dominates the cooling rate for $T \gtrsim 10^7 \text{ K}$ and for which the cooling rate is given by (Osterbrock 1989):

$$\Lambda \simeq 7.99 \times 10^{-24} \text{ erg cm}^{-3} \text{ s}^{-1} \left(\frac{n_{\text{H}}}{1 \text{ cm}^{-3}} \right)^2 \left(\frac{T}{10^{7.5} \text{ K}} \right)^{1/2} \times \\ g_{\text{f}} \eta_{\text{e}} (\eta_{\text{HII}} + \eta_{\text{HeII}} + \eta_{\text{HeIII}}) \\ \simeq 1.12 \times 10^{-23} \text{ erg cm}^{-3} \text{ s}^{-1} \left(\frac{n_{\text{H}}}{1 \text{ cm}^{-3}} \right)^2 \left(\frac{T}{10^{7.5} \text{ K}} \right)^{1/2}$$

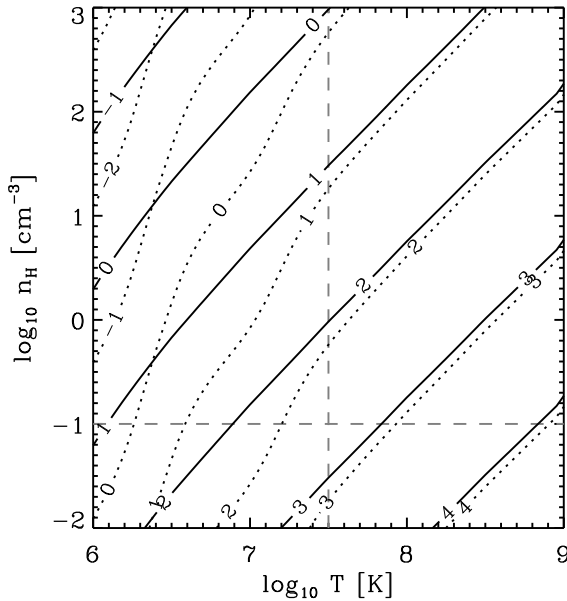


Figure 1. Contour plot of the logarithm of the ratio between the cooling time and the sound-crossing time over the SPH kernel as a function of the density and the temperature of the gas. The cooling time scale is computed using tabulated cooling rates for primordial (solid contours) and solar (dotted contours) element abundances and assuming collisional ionisation equilibrium. We show the ratio for the particle mass used in our simulations of the $10^{12} h^{-1} M_{\odot}$ halo. The vertical dashed line marks the fiducial heating temperature of $10^{7.5}$ K and the horizontal dashed line the star formation density threshold in our simulations.

$$\frac{(1 + X_H)(1 + 3X_H)}{8X_H^2}, \quad (12)$$

where $\eta_i = n_i/n_H$ is the number density of species i relative to hydrogen and we assumed the plasma to be fully ionised in the last step. We assumed for simplicity that the Gaunt factor $g_f \simeq 1.4$ (consistent with the approximated equation given by Theuns et al. (1998) for our fiducial temperature increase) and a primordial composition. Hence, we obtain a radiative cooling time of

$$t_c \simeq 3.26 \times 10^7 \text{ yr} \left(\frac{n_H}{1 \text{ cm}^{-3}} \right)^{-1} \left(\frac{T}{10^{7.5} \text{ K}} \right)^{1/2} \times \left(\frac{\mu}{0.6} \right)^{1/2} \left(\frac{f(X_H)}{0.13} \right), \quad (13)$$

where

$$f(X_H) = X_H(1 + X_H)^{-1}(1 + 3X_H)^{-1} \quad (14)$$

and $f(X_H = 0.752) \simeq 0.13$.

Thus, we can write for the ratio between the two time scales

$$\frac{t_c}{t_s} = 2.8 \times 10^2 \left(\frac{n_H}{1 \text{ cm}^{-3}} \right)^{-1} \left(\frac{T}{10^{7.5} \text{ K}} \right) \left(\frac{h}{100 \text{ pc}} \right)^{-1} \times \left(\frac{\mu}{0.6} \right)^{-3/2} \left(\frac{f(X_H)}{0.13} \right), \quad (15)$$

For the case of SPH simulations, the spatial resolution

is given by the gas particle’s smoothing kernel which can be approximated as

$$h \simeq \left(\frac{3}{4\pi} \frac{\sum_{i=1}^{N_{\text{ngb}}} m_i}{\rho} \right)^{1/3} \simeq \left(\frac{3}{4\pi} \frac{N_{\text{ngb}} \langle m \rangle}{m_H n_H} X_H \right)^{1/3}, \quad (16)$$

where $\langle m \rangle$ is the average mass of the gas particles. Substituting the above approximation into equation (15) we obtain the ratio of time scales

$$\frac{t_c}{t_s} \simeq 98 \left(\frac{n_H}{1 \text{ cm}^{-3}} \right)^{-2/3} \left(\frac{T}{10^{7.5} \text{ K}} \right) \left(\frac{\langle m \rangle}{7 \times 10^4 M_{\odot}} \right)^{-1/3} \times \left(\frac{N_{\text{ngb}}}{48} \right)^{-1/3} \left(\frac{\mu}{0.6} \right)^{-3/2} \left(\frac{g(X_H)}{0.14} \right), \quad (17)$$

where $g(X_H) = X_H^{-1/3} f(X_H)$ and we used the particle mass appropriate for our simulations of the $10^{12} h^{-1} M_{\odot}$ halo.

We expect cooling losses to be important for $t_c \lesssim t_s$. The exact value of the ratio $f_t \equiv t_c/t_s$ required to ensure efficient feedback can only be determined using simulations, but we expect it to be similar to 10 and will therefore use this as our fiducial value. This agrees well with the recent, independent work of Creasey et al. (2011), who derived a resolution criterion for shock capturing in SPH and adaptive mesh refinement (AMR) simulations. Their criterion is based on comparing the rates of shock heating and radiative cooling in a shock front, and ensures that shock heating overwhelms cooling in order to avoid numerical over-cooling. Following the suggestion of DS08, they applied their results to the injection of thermal energy, and obtained a criterion that basically translates into $t_c/t_s > 8$.³

From the relation between the sound crossing time and the Courant time step, one can estimate the number of simulation time steps it would take the gas to radiate its thermal energy if it cooled isochorically: $n_{\text{step}} \sim t_c/\Delta t = f_t t_s/\Delta t = f_t/C$ (~ 30 for the fiducial value of f_t and $C = 0.3$). In most implementations of SPH the sound speed in the Courant criterion is replaced by a “signal velocity” (e.g. Monaghan 1997), $v_{\text{sig}} \gtrsim 2c_s$, which would more than double the number of time steps.

Inverting equation (17), we find the following maximum density for which the feedback is expected to be effective,

$$n_{H, t_c = f_t t_s} = 31 \text{ cm}^{-3} \left(\frac{T}{10^{7.5} \text{ K}} \right)^{3/2} \left(\frac{f_t}{10} \right)^{-3/2} \times \left(\frac{\langle m \rangle}{7 \times 10^4 M_{\odot}} \right)^{-1/2} \left(\frac{N_{\text{ngb}}}{48} \right)^{-1/2} \times \left(\frac{\mu}{0.6} \right)^{-9/4} \left(\frac{g(X_H)}{0.14} \right)^{3/2}. \quad (18)$$

The critical density is thus proportional to $T^{3/2} \langle m \rangle^{-1/2}$.

For the case of AMR simulations, the spatial resolution is given by the linear size of the grid cell, which is commonly decreased until it is some factor, f_J , smaller than the local Jeans length: $h \leq L_J/f_J$. Expressing the Jeans length as a function of temperature and density, $L_J \equiv c_s \sqrt{\pi/(G\rho)}$, and

³ Note that Creasey et al. (2011) derived their criterion by estimating the velocity of a blast wave at the blast radius of half the mean inter-particle distance.

substituting this into equation (15), we obtain

$$\frac{t_c}{t_s} \geq 50 \left(\frac{n_H}{1 \text{ cm}^{-3}} \right)^{-1/2} \left(\frac{T}{10^{7.5} \text{ K}} \right) \left(\frac{T_0}{10^4 \text{ K}} \right)^{-1/2} \left(\frac{f_J}{4} \right) \times \left(\frac{\mu}{0.6} \right)^{-1} \left(\frac{g'(X_H)}{0.15} \right), \quad (19)$$

where T_0 is the initial gas temperature (from which the Jeans mass, hence the spatial resolution, is derived), $g'(X_H) = X_H^{-1/2} f(X_H)$, and we assumed that the Jeans length is resolved with four resolution elements. The equality holds for $h = L_J/f_J$. Note that the same relation applies to SPH simulations with particle mass at least f_J^3 times smaller than the Jeans mass in gas with density n_H and temperature T_0 .

Inverting equation (19), we obtain

$$n_{H, t_c = f_J t_s} \geq 25 \text{ cm}^{-3} \left(\frac{T}{10^{7.5} \text{ K}} \right)^2 \left(\frac{T_0}{10^4 \text{ K}} \right)^{-1} \left(\frac{f_J}{4} \right)^2 \times \left(\frac{\mu}{0.6} \right)^{-2} \left(\frac{g'(X_H)}{0.15} \right)^2, \quad (20)$$

which is the analogue of equation (18) for AMR (and for SPH simulations with particle mass at least f_J^3 times smaller than the Jeans mass in gas with density n_H and temperature T_0).

We show in Fig. 1 a contour plot of the time-scale ratio t_c/t_s in the temperature-density plane for the fiducial gas particle mass $m_g = 5.1 \times 10^4 h^{-1} M_\odot$. We computed t_c using the tabulated values of the collisional cooling rates of (Wiersma, Schaye, & Smith 2009a), which are also used in the SPH simulations described below. We combine in the same plot the two cases of primordial (solid contours) and solar (dotted contours) chemical compositions. The vertical dashed line marks the fiducial heating temperature of $10^{7.5} \text{ K}$, while the horizontal dashed line indicates the density threshold for SF in our simulations. For $T \geq 10^{7.5} \text{ K}$ the difference between primordial and solar metallicity is very small, but at lower temperatures metals reduce the ratio t_c/t_s . Once the temperature has dropped to 10^7 K for the case of solar abundances (or to values smaller than 10^6 K for primordial abundances), collisional excitation processes cause the cooling rate to increase as the temperature drops (e.g. Wiersma, Schaye, & Smith 2009a). For such temperatures the equations above, which assumed the cooling rate to be dominated by Bremsstrahlung, will underestimate the radiative losses and will therefore overestimate the minimum density for which the feedback is expected to be efficient.

Interestingly, for purely adiabatic expansion, i.e. $\rho \propto T^{3/2}$, the ratio t_c/t_s remains constant for the case of SPH (eq. [17]). In that case the gas will follow a track parallel to the high temperature part of the contours in Fig. 1 and $t_c \propto \rho^{-2/3}$. Hence, if radiative losses were unimportant initially, so that the hot bubble will start to expand adiabatically, then radiative losses will remain unimportant as long as the cooling rate is dominated by Bremsstrahlung. For AMR, on the other hand, the ratio $t_c/t_s \propto T^{1/4}$ during the adiabatic phase, which implies that radiative losses may already become important while Bremsstrahlung dominates.

5 SIMULATIONS

We ran simulations of isolated disc galaxies embedded in dark matter haloes with total masses of 10^{10} and $10^{12} h^{-1} M_\odot$, where $h = 0.73$. The initial conditions are as in Schaye & Dalla Vecchia (2008) and DS08, thus the models do not include gaseous haloes and all the gas is initially in the discs. We adopted a larger gravitational softening length than in the previous works for the massive galaxy. We also modified the original code as described below.

5.1 Code and initial conditions

We use a modified version of the TreePM/SPH code GADGET (Springel 2005) for all the simulations presented in this paper.

We employ the SF recipe of Schaye & Dalla Vecchia (2008), which we briefly describe here. Gas denser than the critical density for the onset of the thermo-gravitational instability ($n_H \sim 10^{-2} - 10^{-1} \text{ cm}^{-3}$) is expected to be multi-phase and star-forming (Schaye 2004). We model such gas by imposing a minimum temperature floor given by an effective equation of state with pressure $P \propto \rho_g^{\gamma_{\text{eff}}}$ for densities exceeding $n_H = 0.1 \text{ cm}^{-3}$, normalised to $P/k = 10^3 \text{ cm}^{-3} \text{ K}$ at the threshold. We use $\gamma_{\text{eff}} = 4/3$ for which both the Jeans mass and the ratio of the Jeans length and the SPH kernel are independent of the density, thus preventing spurious fragmentation due to a lack of numerical resolution.

We introduce a different definition of star-forming particle. In the previous works a gas particle was flagged as star-forming if it crossed the density threshold $n_H^* = 0.1 \text{ cm}^{-3}$ while its temperature was below $T = 10^5 \text{ K}$. The particle then remained star-forming until its density fell below the threshold density or the particle was promoted to a wind particle.

In the present work we proceed as follows. Each particle is free to cool to lower temperatures, but not below the temperature T_{EoS} imposed by the effective equation of state. A gas particle is star-forming if

$$\begin{cases} n_H \geq n_H^* \\ \log_{10} T < \log_{10} T_{\text{EoS}} + \Delta \log_{10} T_{\text{EoS}} \end{cases}, \quad (21)$$

where $\Delta \log_{10} T_{\text{EoS}}$ is a free parameter which we set to $\Delta \log_{10} T_{\text{EoS}} = 0.5$ dex.

The Kennicutt-Schmidt SF law is analytically converted and implemented as a pressure law. As we demonstrated in Schaye & Dalla Vecchia (2008), our method allows us to reproduce arbitrary input SF laws for any equation of state without tuning any parameters. We use the observed Kennicutt (1998) law

$$\dot{\Sigma}_* = 1.5 \times 10^{-4} M_\odot \text{ yr}^{-1} \text{ kpc}^{-2} \left(\frac{\Sigma_g}{1 M_\odot \text{ pc}^{-2}} \right)^{1.4}, \quad (22)$$

where the different normalisation accounts for the fact that we are using a Chabrier IMF.

Radiative cooling and heating were included using tables for hydrogen and helium from Wiersma, Schaye, & Smith (2009a). The cooling tables were generated using the publicly available package CLOUDY (version 07.02; Ferland 2000), assuming ionisation equilibrium in the presence of the Haardt & Madau (2001) model

Table 1. Simulation parameters: total mass, M_{halo} ; fraction of SN energy injected, f_{th} ; temperature jump, $\log_{10} \Delta T$; total number of particles, N_{tot} ; total number of gas particles in the disc, N_{disc} ; mass of baryonic particles, m_b ; mass of dark matter particles, m_{DM} ; gravitational softening of baryonic particles, ϵ_b ; gravitational softening of dark matter particles, ϵ_{DM} ; thermal feedback included, (Feedback). Values different from the fiducial ones are shown in bold.

Simulation	M_{halo} ($h^{-1} \text{ M}_{\odot}$)	f_{th}	$\log_{10} \Delta T$ (K)	N_{tot}	N_{disc}	m_b ($h^{-1} \text{ M}_{\odot}$)	m_{DM} ($h^{-1} \text{ M}_{\odot}$)	ϵ_b ($h^{-1} \text{ pc}$)	ϵ_{DM} ($h^{-1} \text{ pc}$)	Feedback
<i>G10-NOFB</i>	10^{10}	—	—	5 000 494	235 294	5.1×10^2	2.4×10^3	10	17	N
<i>G10-040-70</i>	10^{10}	0.4	7.0	5 000 494	235 294	5.1×10^2	2.4×10^3	10	17	Y
<i>G10-100-65</i>	10^{10}	1.0	6.5	5 000 494	235 294	5.1×10^2	2.4×10^3	10	17	Y
<i>G10-100-70</i>	10^{10}	1.0	7.0	5 000 494	235 294	5.1×10^2	2.4×10^3	10	17	Y
<i>G10-100-75</i>	10^{10}	1.0	7.5	5 000 494	235 294	5.1×10^2	2.4×10^3	10	17	Y
<i>G10-100-80</i>	10^{10}	1.0	8.0	5 000 494	235 294	5.1×10^2	2.4×10^3	10	17	Y
<i>G10-100-85</i>	10^{10}	1.0	8.5	5 000 494	235 294	5.1×10^2	2.4×10^3	10	17	Y
<i>G10-100-75-LR08</i>	10^{10}	1.0	7.5	625 061	29 411	4.1×10^3	1.9×10^4	20	34	Y
<i>G10-100-75-LR64</i>	10^{10}	1.0	7.5	78 132	3 676	3.3×10^4	1.5×10^5	40	68	Y
<i>G12-NOFB</i>	10^{12}	—	—	5 000 494	235 294	5.1×10^4	2.4×10^5	46	79	N
<i>G12-040-70</i>	10^{12}	0.4	7.0	5 000 494	235 294	5.1×10^4	2.4×10^5	46	79	Y
<i>G12-100-65</i>	10^{12}	1.0	6.5	5 000 494	235 294	5.1×10^4	2.4×10^5	46	79	Y
<i>G12-100-70</i>	10^{12}	1.0	7.0	5 000 494	235 294	5.1×10^4	2.4×10^5	46	79	Y
<i>G12-100-75</i>	10^{12}	1.0	7.5	5 000 494	235 294	5.1×10^4	2.4×10^5	46	79	Y
<i>G12-100-80</i>	10^{12}	1.0	8.0	5 000 494	235 294	5.1×10^4	2.4×10^5	46	79	Y
<i>G12-100-85</i>	10^{12}	1.0	8.5	5 000 494	235 294	5.1×10^4	2.4×10^5	46	79	Y
<i>G12-100-75-LR08</i>	10^{12}	1.0	7.5	625 061	29 411	4.1×10^5	1.9×10^6	92	158	Y
<i>G12-100-75-LR64</i>	10^{12}	1.0	7.5	78 132	3 676	3.3×10^6	1.5×10^7	184	316	Y

for the $z = 0$ UV background radiation from quasars and galaxies, and the cosmic microwave background.

We implemented a version of the time-stepping algorithm described by Durier & Dalla Vecchia (2012). Inactive particles that receive feedback energy are immediately activated so that they can respond promptly to their new energetic state. Their and their active neighbours' signal velocities (see e.g. Monaghan 1997) are also updated in order to calculate the size of the next time-step consistently. The new time-step is then propagated to the inactive neighbours following the scheme of Saitoh & Makino (2009). We refer the reader to Durier & Dalla Vecchia (2012) for a detailed discussion of the benefits introduced by the scheme.

However, we do not expect the integration accuracy of our simulations to improve significantly compared with e.g. DS08. As argued by Durier & Dalla Vecchia (2012), imposing a limit to the maximum allowed time-step (e.g., by significantly reducing the gravitational softening, as we have done here and in DS08), may also maintain good energy conservation in the case of strong energy perturbations. Indeed, we found only small deviations in the global properties of the outflows when running the same fiducial models without the time-step limiter.

The initial conditions are based on the model of Springel, Di Matteo, & Hernquist (2005) and are described in DS08. The model consists of a dark matter halo, a stellar bulge, and an exponential disc of stars and gas. The circular velocities at the virial radii are 35.1 and 163 km s^{-1} for the 10^{10} and $10^{12} h^{-1} \text{ M}_{\odot}$ haloes, respectively. The virial radii are 35.1 and 163 $h^{-1} \text{ kpc}$. The halo is rotating and has a dimensionless spin parameter $\lambda = 0.33$. The disc contains 4 percent of both the total mass and the total angular momentum. The bulge contains 1.4 percent of the total mass and has a scale length one tenth of that of the disc. The bulge

has no net rotation. The initial gas fraction of the disc is 30 percent, the remaining 70 percent of the disc mass is made up of stars. The vertical distribution of the stellar disc has a constant scale height of 10 percent of the radial disc scale length.

Except for our low-resolution runs, the total number of particles in each simulation is 5,000,494, of which 235,294 are gas particles in the disc. The baryonic particle mass for the $10^{10} h^{-1} \text{ M}_{\odot}$ ($10^{12} h^{-1} \text{ M}_{\odot}$) halo is $m_b = 5.1 \times 10^2 h^{-1} \text{ M}_{\odot}$ ($m_b = 5.1 \times 10^4 h^{-1} \text{ M}_{\odot}$). The gravitational softening length was set to $\epsilon_b = 10 h^{-1} \text{ pc}$ for the baryons and to $(m_{\text{DM}}/m_b)^{1/3} \epsilon_b \approx 17 h^{-1} \text{ pc}$ for the dark matter in the $10^{10} h^{-1} \text{ M}_{\odot}$ halo. The softening for the massive galaxy is scaled up in proportion to $m_{\text{DM}}^{1/3}$.

5.2 Simulation parameters

Table 1 lists the simulations we have performed. Each simulation was evolved for 500 Myr. The simulations are labelled with the prefix *G10* and *G12* for the 10^{10} and the $10^{12} h^{-1} \text{ M}_{\odot}$ haloes, respectively, followed by the percentage of the SN energy that is injected and by the logarithm of the temperature increase. For example, *G10-040-75* refers to the $10^{10} h^{-1} \text{ M}_{\odot}$ halo, with the SN feedback injecting 40% of the total available energy and increasing the gas particle temperature by $\Delta T = 10^{7.5} \text{ K}$. We have run several variations of the fiducial models, *G10-100-75* and *G12-100-75*. The list of all the models follows:

- One run without SN feedback (*G[10,12]-NOFB*).
- One run injecting 40 percent of the available SN energy, *G[10,12]-040-75*. This is used for comparison with the kinetic feedback simulations of DS08, which also used 40 percent of the energy.

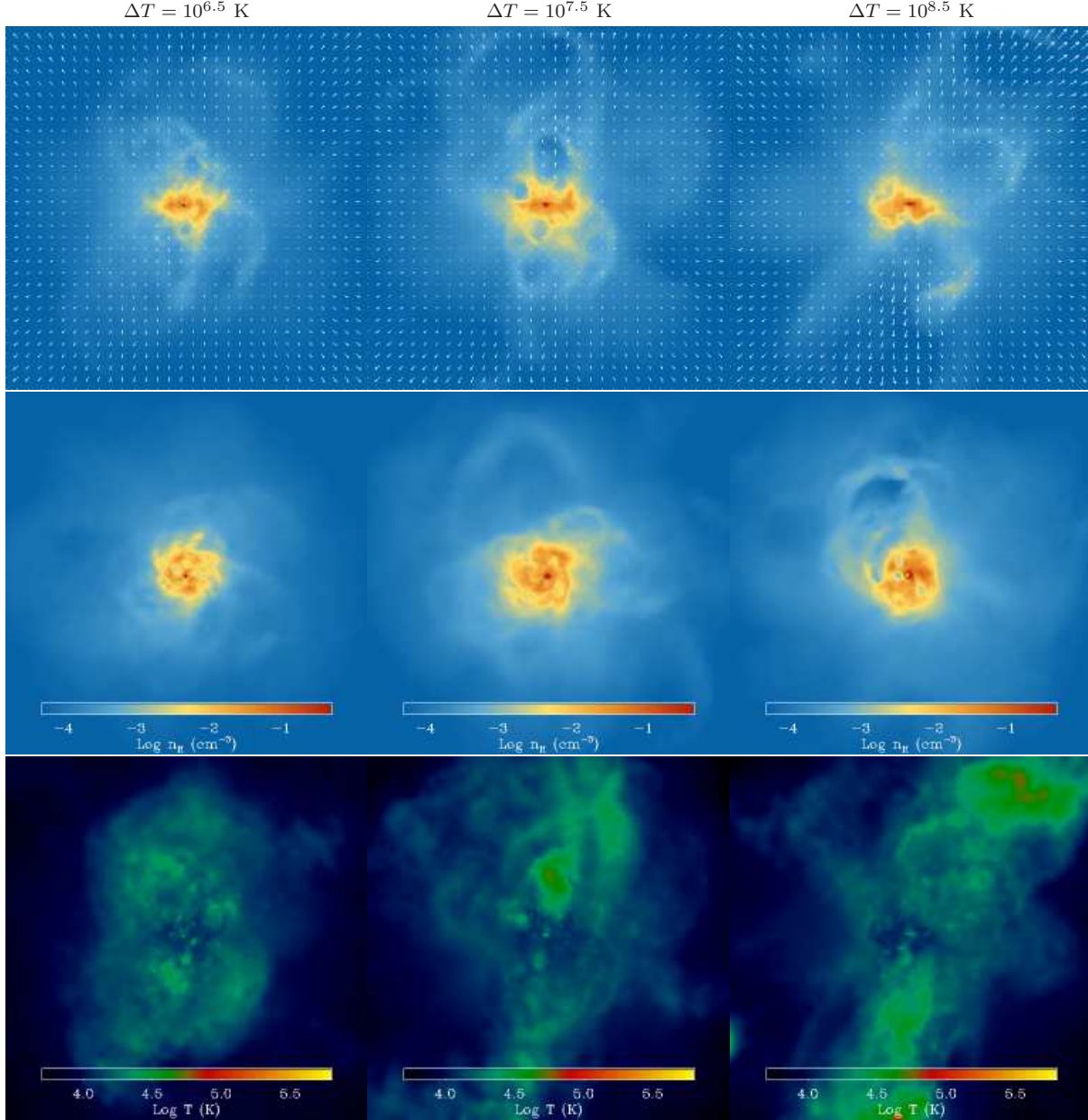


Figure 2. Projections of the gas density (top row: edge-on; middle row: face-on) and temperature (bottom-row: edge-on) for models *G10-100-65* (left column), the fiducial model *G10-100-75* (middle column) and *G10-100-85* (right column) at time $t = 250$ Myr. The white arrows in the top row show the velocity field. Images are $17.5h^{-1}$ kpc on a side. The colour coding is logarithmic in density ($-4.3 < \log_{10} n_{\text{H}}/\text{cm}^{-3} < -0.3$) and temperature ($3.7 < \log_{10} T/\text{K} < 5.8$). The colour scale is indicated by the colour bars in each column.

- One set of runs varying the temperature increase $\log_{10} \Delta T = [6.5, 7.0, 7.5, 8.0, 8.5]$. These runs are labelled $G[10,12]-100-[65, 70, 75, 80, 85]$, respectively.
- Two runs in which the number of particles was decreased by factors of 8 and 64, respectively ($G[10,12]-100-75\text{-LR}08$, $G[10,12]-100-75\text{-LR}64$).

To eliminate differences other than the feedback recipe from the comparison with DS08, we repeated the simulations of models *m12* and *m12nowind* of DS08 with the new version of the code. We changed the softening to the one used in this work, and used the time-step limiter for the feedback run.

6 SIMULATION RESULTS

In this section we describe tests of our implementation of thermal feedback. We first show the effect of varying the temperature increase. We proceed with a comparison to the kinetic feedback model of DS08. We conclude the section by reporting the results of resolutions tests.

6.1 Dependence on the temperature increase

We ran a set of simulations with $f_{\text{th}} = 1$ and varying $\log_{10} \Delta T = [6.5, 7.0, 7.5, 8.0, 8.5]$ to study the dependence on the temperature increase. We first describe the morphol-

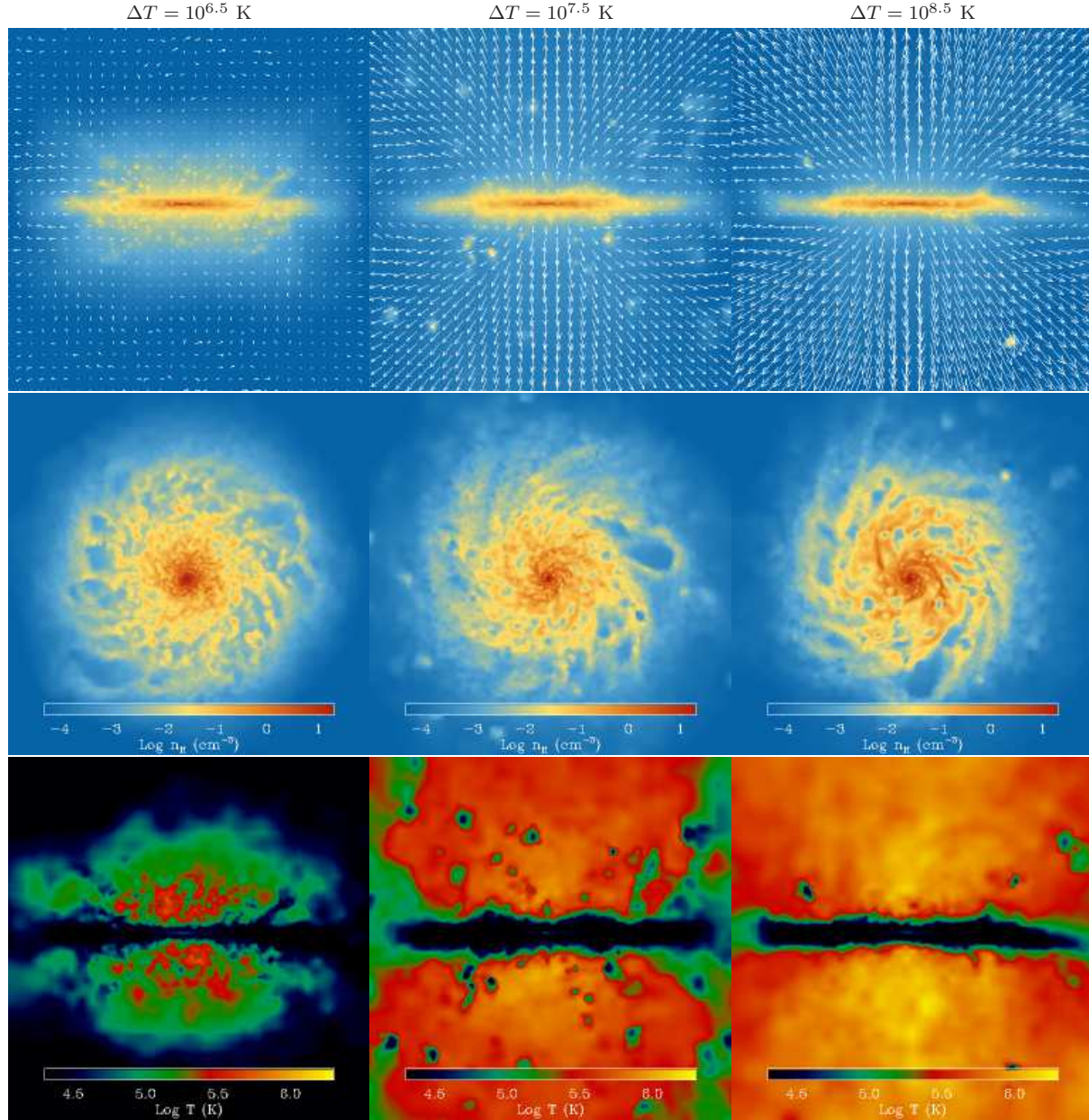


Figure 3. Projections of the gas density (top row: edge-on; middle row: face-on) and temperature (bottom-row: edge-on) for models *G12-100-65* (left column), the fiducial model *G12-100-75* (middle column) and *G12-100-85* (right column) at time $t = 250$ Myr. The white arrows in the top row show the projected velocity field. Images are $45h^{-1}$ kpc on a side. The colour coding is logarithmic in density ($-4.3 < \log_{10} n_{\text{H}}/\text{cm}^{-3} < 1.3$) and temperature ($4.3 < \log_{10} T/\text{K} < 6.3$). The colour scale is indicated by the colour bars in each column.

ogy of the galaxies and their outflows, and proceed with discussing the SF histories and the outflow properties quantitatively.

6.1.1 Morphology

For each halo, we compare here the fiducial model, which has $\log_{10} \Delta T = 7.5$, to our most extreme models, which use $\log_{10} \Delta T = [6.5, 8.5]$. Fig. 2 shows projections of the density (top and middle rows) and temperature (bottom row) for the dwarf galaxy at time $t = 250$ Myr for three different values of the temperature increase (from left to right, $\log_{10} \Delta T =$

$[6.5, 7.5, 8.5]$). Recall that all models inject the same amount of energy per unit stellar mass.

The morphology of the galaxy is irregular in all cases. As the heating temperature is increased, the low-density bubbles in the ISM and in the circumgalactic medium increase in size and open up vertical channels through which the outflows can escape. Consequently, the outflow becomes more collimated along the vertical axis as ΔT increases, enhancing its bipolarity. The velocity field overplotted in the top row shows that the flow is faster for larger ΔT , while the bottom row shows that the outflowing gas is also hotter.

Fig. 3 shows edge-on projections of the density (top

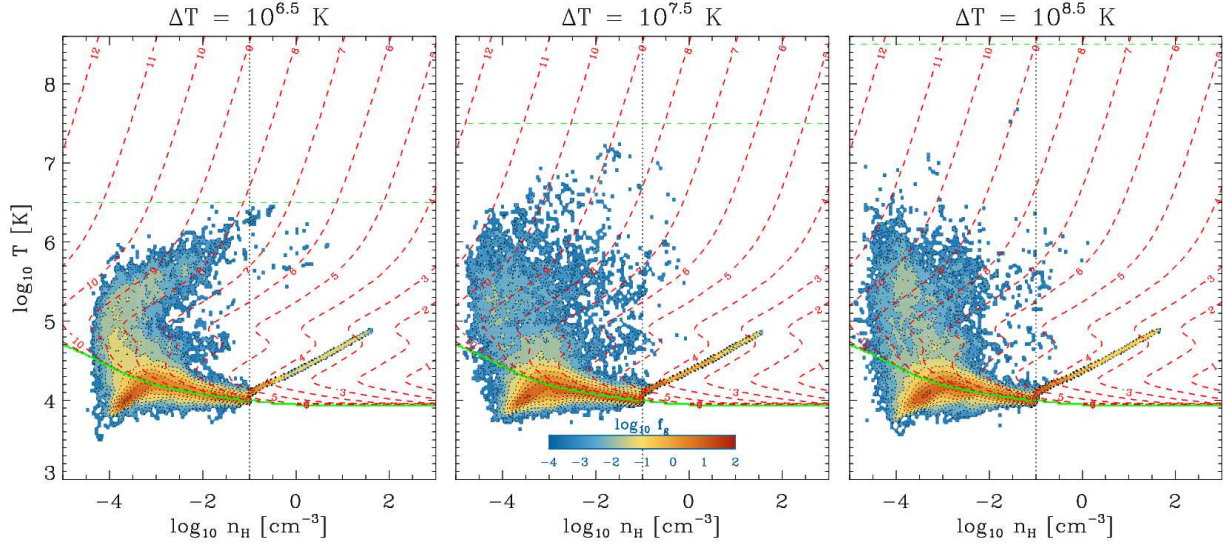


Figure 4. Two-dimensional mass-weighted probability density distribution of the gas within $0.2r_{\text{vir}}$ of the dwarf galaxy in temperature-density space at time $t = 250$ Myr. The colour coding indicates $f_g = (dM/M)/d \log_{10} n_H / d \log_{10} T$. The three panels correspond to the same three models as were shown in Fig. 2. The twelve contours of f_g (black, dotted) are equally spaced in the range showed by the colour bar. The red, dashed curves indicate radiative cooling time contours and their labels indicate $\log_{10}(t_c/\text{yr})$. Below the solid, green line photo-heating by the UV background dominates over radiative cooling. The horizontal, dashed line indicates the heating temperature ΔT . The vertical, dotted line marks the threshold for star formation. The imposed, effective equation of state is visible for densities larger than the threshold density.

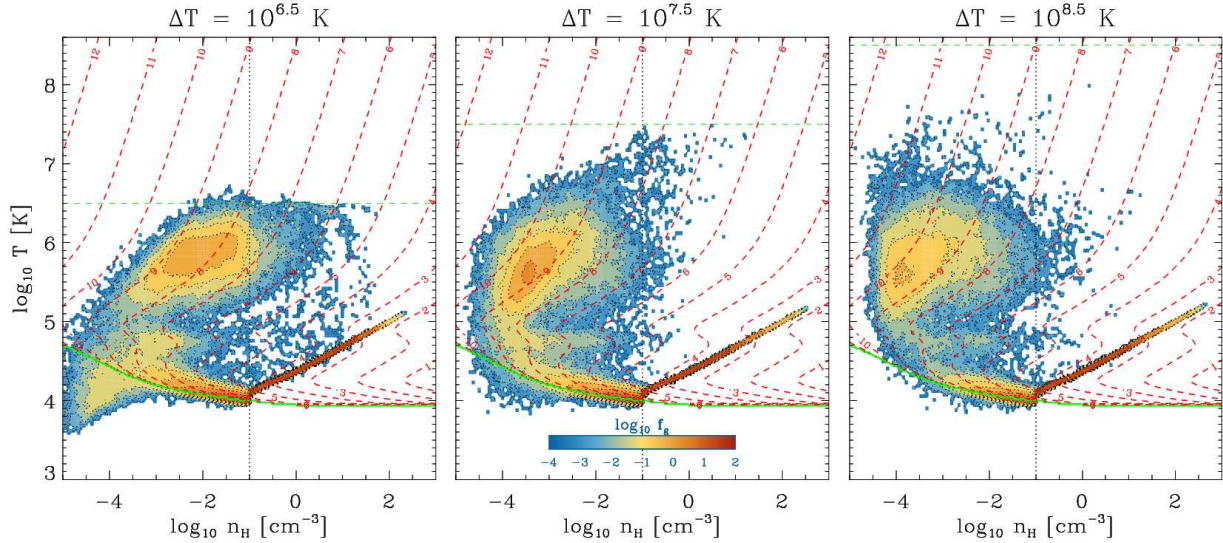


Figure 5. As Fig. 4, but for the models of the massive galaxy shown in Fig. 3.

row) and temperature (bottom row) for the massive galaxy for the same three different values of the temperature increase. The dependence on ΔT is more evident for this more massive galaxy. For $\Delta T = 10^{6.5}$ K (left column), most of the outflowing gas is confined to a region around the disc. The disc looks puffed up as the expelled gas is deposited just outside it, and the gas breaks up in little blobs. The velocities are small and the velocity field does not show a clear preferential orientation. There is a galactic fountain, but no large-scale galactic wind.

In contrast, the fiducial model ($\Delta T = 10^{7.5}$ K; middle column) shows a clear bipolar outflow, which is sustained until the end of the run. The outflow is mostly driven from the inner part of the disc where a large fraction of the SF is taking place, and it is collimated by the disc which impedes motion within its plane. The temperature map shows several cold blobs above and below the galactic disc. The blobs come from the disc and are moving outward, thus the outflow is ejecting parcels of cold gas. Cold blobs are seen falling back onto the disc at large radii.

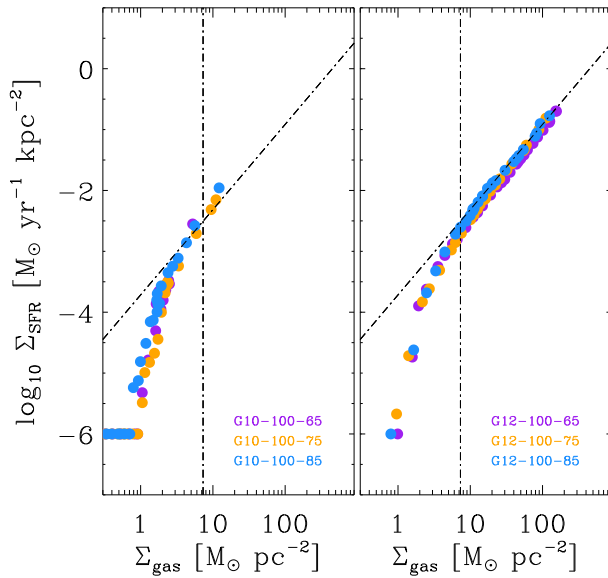


Figure 6. The Kennicutt-Schmidt SF relation for a selection of *G10* (left panel) and *G12* (right panel) models at $t = 250$ Myr. Surface densities are computed in cylindrical annuli containing a constant number of particles and including all particles with vertical coordinate $|z| < 2$ kpc. The tilted line shows the observed Kennicutt SF law, equation (22), whereas the vertical line shows the gas surface density below which SF is observed to become inefficient (for more details see Schaye & Dalla Vecchia 2008). All models are in excellent agreement with the observations.

The highest ΔT run ($\Delta T = 10^{8.5}$ K; right column) looks similar to the fiducial model, but the wind is hotter and moving faster and the circumgalactic medium contains fewer cold blobs.

Videos illustrating the time evolution of the model galaxies are available at this web address: <http://www.strw.leidenuniv.nl/DS12/>

6.1.2 Gas phase distribution

The mass-weighted probability distribution function (PDF) of the gas at $t = 250$ Myr in the (n_H, T) plane is shown in Figs. 4 and 5 for the models shown in Figs. 2 and 3, respectively. To limit the effects of the vacuum boundary conditions (mainly adiabatic cooling to extremely low temperatures and densities), we include only the gas inside a spherical volume of radius $0.2r_{\text{vir}}$, but we normalise the PDFs to the total gas mass. The vertical, dotted line marks our threshold density for SF, and at higher densities the imposed, effective equation of state is clearly visible. Contours of constant radiative cooling time (dashed, red lines) are over-plotted.⁴ The contour labels indicate integer values of $\log_{10}(t_c/\text{yr})$. The equilibrium between radiative cooling and photo-heating by the UV background is shown by the solid, green curve. Below this curve radiative heating dominates

over radiative cooling. Note that gas can reach temperatures lower than the equilibrium value if it cools adiabatically. In the absence of feedback, none of the gas below the SF threshold would have temperatures significantly above the equilibrium value. Finally, the horizontal, dashed (green) lines indicate the feedback heating temperatures ΔT . Gas in which feedback energy has been injected initially resides near these lines and, as long as radiative cooling is unimportant, will expand adiabatically, exiting the star-forming region at different temperatures. Indeed, the phase diagrams show different distributions of shock-heated gas for different ΔT , with the low-density, high-temperature regions being more populated for increasing ΔT .

For the dwarf galaxy (Fig. 4) the temperature-density distributions are similar for all values of ΔT , although there are some differences in the high temperature regime. We will show later that the SF histories and the outflows are also very similar for all values of ΔT and that, given the resolution, this is in accord with the results of section 4. There is very little hot gas. The surface density of the disc, and hence the pressure, is too low to confine the heated gas, which therefore immediately blows out of the disc and cools adiabatically.

For the massive galaxy changing ΔT has a much more dramatic impact on the distribution of shock-heated gas ($T > 10^5$ K). For the model with the lowest value of ΔT (left panel of Fig. 5), the peak of the PDF lies within the density range 10^{-3} to 10^{-2} cm^{-3} . This confirms the qualitative result shown in Fig. 3: most of the outflowing gas accumulates in a region around the disc. If we increase ΔT (middle and right panels), the peak in the PDF moves to lower densities ($\sim 10^{-4}$ cm^{-3}) thanks to the development of a large-scale outflow that moves gas away from the disc. The total fraction of shock-heated gas decreases with the ΔT because less gas resides within $0.2r_{\text{vir}}$ if the wind velocity is higher.

6.1.3 Star formation history

Before discussing the SF histories, we show the predicted Kennicutt-Schmidt SF relations in Fig. 6. The left (right) panel shows the same three different models as were shown in Fig. 2 (Fig. 3) for the dwarf (massive) galaxy. Gas mass and SF surface densities were computed in annuli containing a constant number of gas particles and including all particles with vertical coordinate $|z| < 2$ kpc. The observed Kennicutt-Schmidt law (eq. (22); tilted line) and the steepening at the SF threshold density (vertical line) are well matched. This success is not unexpected, as we already showed in Schaye & Dalla Vecchia (2008) that the observed SF law can be implemented directly in the form of a pressure law and that this enables the simulations to reproduce the observations without the need to tune any parameters and irrespective of whether strong feedback is present. While feedback determines the surface density of the gas, it does not affect the efficiency of star formation at a fixed surface density in our models, since pressure and surface density are closely related in self-gravitating systems.

The dependence of the SF histories on ΔT is shown in Fig. 7. For the dwarf galaxy (left panel), the star formation rate (SFR) drops sharply within the first 100 Myr due to the strong feedback produced by the initial burst of SF, and

⁴ Note that the t_c contours have been calculated assuming a constant mean molecular weight, $\mu = 0.6$.

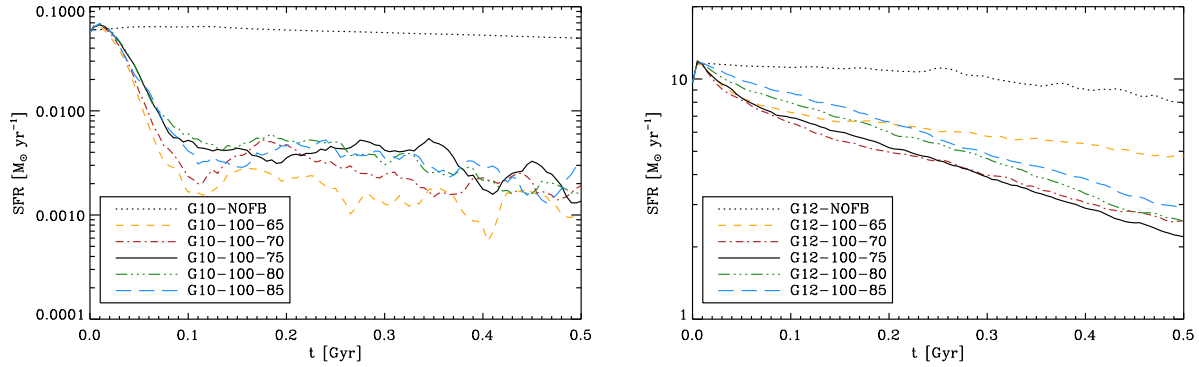


Figure 7. SFR as a function of time for the galaxies in the 10^{10} and the $10^{12} h^{-1} M_{\odot}$ haloes (left- and right panels, respectively). We vary the temperature increase due to feedback events in steps of 0.5 dex over the range $\log_{10} \Delta T / \text{K} = [6.5, 8.5]$. The dwarf galaxy’s SF history is insensitive to the value of ΔT , while for the massive galaxy the feedback is less efficient for the lowest heating temperature.

remains nearly constant thereafter. The fact that the sharp drop is due to feedback can be seen by comparing to the nearly horizontal black, dotted curve, which shows the SF history for a run without feedback. The factor by which the feedback reduces the SFR is insensitive to ΔT . This is in accord with the calculations presented in Section 4. The dwarf galaxy has a low surface density and forms most of its stars at densities close to the SF threshold of $n_{\text{H}} = 10^{-1} \text{ cm}^{-3}$ (see Fig. 4). For such densities and primordial abundances we expect cooling losses to be small even for heating temperatures as low as $10^{6.5} \text{ K}$. Indeed, for our particle mass of $7 \times 10^2 M_{\odot}$ and a heating temperature of $T = 10^{6.5} \text{ K}$, equation (18) tells us that cooling losses should be unimportant for densities $n_{\text{H}} < 10 \text{ cm}^{-3}$.

However, as Fig. 1 shows, the situation could be different for solar abundances. While the cooling time is insensitive to the metallicity for $T \gtrsim 10^{7.5} \text{ K}$, for $T = 10^{6.5} \text{ K}$ it is about an order of magnitude smaller for solar metallicity than it is for primordial abundances. A factor ten increase in the cooling rate would reduce the maximum density for which the feedback is expected to be effective to $n_{\text{H}} \approx 0.3 \text{ cm}^{-3}$ (eqs. [17] and [18]). We would therefore expect a significant fraction of the feedback energy to be radiated away before it can be converted into kinetic form, if we were to run the dwarf galaxy simulation with $\Delta T = 10^{6.5} \text{ K}$ and solar metallicity. Indeed, we have performed such a run (not shown) and find the SFR to be much higher. After 400 Myr it is about $0.04 M_{\odot} \text{ yr}^{-1}$ which is closer to the run without feedback than to the run with the same ΔT but primordial abundances.

For the massive galaxy the decline in the SFR is more gradual (right panel). After a few hundred Myr, all runs predict roughly the same SFR except for the one adopting $\Delta T = 10^{6.5} \text{ K}$, which has a substantially higher SFR. The morphological comparison (Fig. 3) shows that in this run the gas is unable to escape to large radii. Instead, it accumulates around the disc, and eventually falls back onto it. This is expected, because equation (18) shows that radiative losses will become important at densities that are 10 times lower than for the dwarf galaxy, because the particle mass is 100 times higher. Moreover, the densities in the ISM are higher in the massive galaxy, with many star particles forming in gas with densities $n_{\text{H}} \sim 1 - 10 \text{ cm}^{-3}$

(Fig. 5). Comparing these numbers to the maximum density for which cooling losses are small at this resolution, $n_{\text{H}} \lesssim 31 \text{ cm}^{-3} (T/10^{7.5})^{3/2}$ (eq. [18]), we expect small changes for $\Delta T = 10^7 \text{ K}$ and a substantial reduction of the feedback efficiency for $\Delta T = 10^{6.5} \text{ K}$.

Models *G12-100-70* and *G12-100-75* have similar SF histories, suggesting convergence of the results. However, models *G12-100-80* and *G12-100-85* have SFRs that are larger than that of the fiducial model by factors of $\simeq 25$ and 40 percent, respectively. The trend for the largest ΔT ’s likely arises from poor sampling of the distribution of SN energy in the disc. Indeed, the expectation value for the number of heated neighbours decreases with ΔT , and is (from eq. [7]) 0.42 and 0.13 for *G12-100-80* and *G12-100-85*, respectively. This shows the importance of locally linking the feedback events with the formation of star particles by depositing the star particle SN energy into at least one of its neighbours. The effect is less severe for the dwarf galaxy because star formation is restricted to smaller scales, these scales are resolved with many more particles, and it is easier to eject gas in this case due to the lower ISM pressure and the shallower gravitational potential well.

Finally, we note that the SFRs are lower than for the kinetic feedback runs of DS08. This difference is, however, due to the different amount of energy injected rather than to the manner in which this is done (i.e. thermal vs. kinetic). We inject more energy here ($f_{\text{th}} = 1$ whereas DS08 used $f_{\text{th}} = 0.4$), thus a stronger quenching is expected. In Section 6.2 we will show that the two methods are in fact in good agreement with each other.

6.1.4 Mass outflow rate and wind velocity

In this section we measure the wind velocity and mass loading as a function of time and radius. We first briefly describe the method, which is identical to the one employed in DS08.

We discretise the following integral equation of the net mass outflow rate through a surface S :

$$\dot{M} = \int_S \rho \mathbf{v} \cdot d\mathbf{S}, \quad (23)$$

where ρ is the gas density and \mathbf{v} is the gas velocity at any position on the surface. Given a spherical shell of radius r

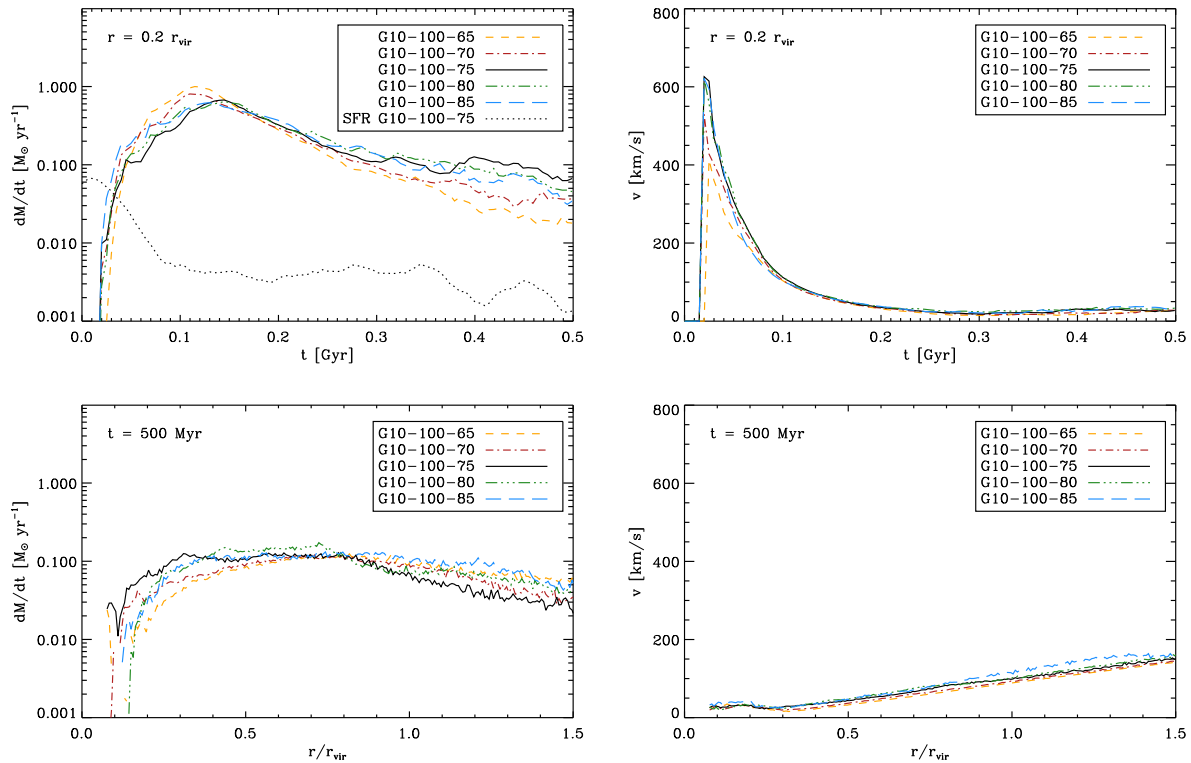


Figure 8. Mass outflow rate (left column) and average outflow velocity (right column) measured through a spherical shell at radius $r = 0.2r_{\text{vir}}$ as a function of time (top row) and at $t = 500$ Myr as a function of radius (bottom row) for models *G10-100-[65,70,75,80,85]*. The dotted line in the top-left panel indicates the SFR of model *G10-100-75*. All other curves are labelled in the legends.

and thickness Δr centred on the origin, the above equation becomes

$$\dot{M}(r, \Delta r) = \frac{1}{\Delta r} \sum_{i=1}^{N_{\text{shell}}} m_i \mathbf{v}_i \cdot \frac{\mathbf{r}_i}{r_i}, \quad (24)$$

where N_{shell} is the total number of particles within the shell, and m_i and \mathbf{r}_i are their mass and position, respectively. We consider all particles and use $\Delta r = r_{\text{vir}}/150$.

The average outflow velocity is also given in discrete form, and is the mass-weighted, average radial velocity:

$$\langle v \rangle(r, \Delta r) = \frac{\sum_{i=1}^{N_{\text{shell}}} m_i (\mathbf{v}_i \cdot \frac{\mathbf{r}_i}{r_i})_+}{\sum_{i=1}^{N_{\text{shell}}} m_i}, \quad (25)$$

where \mathbf{v}_i is the particle velocity. We consider only particles moving away from the origin, as indicated by the subscript “+” in the above equation.

To investigate the dependence of the outflow properties on the temperature increase ΔT , we show in Figs. 8 (dwarf galaxy) and 9 (massive galaxy) the mass outflow rate (left column) and the average outflow velocity (right column). The top row shows the evolution of the wind at radius $r = 0.2r_{\text{vir}}$ and the bottom row shows the dependence on radius at time $t = 500$ Myr.

We first consider the dwarf galaxy (Fig. 8). Apart from the peak velocity, which is reached after only a few tens of Myr, all models look very similar. Apparently, the properties of the wind are nearly independent of the temperature increase ΔT . As discussed in the previous section, this is expected for such a high resolution and for a primordial

composition. However, for solar abundances the equations derived in Section 4 predict that radiative losses do become important for $\Delta T = 10^{6.5}$ K. Indeed, we find that for this heating temperature the mass outflow rate is reduced by more than an order of magnitude if we assume the metallicity to be solar (not shown).

The wind is highly mass-loaded, with mass outflow rates at $0.2r_{\text{vir}}$ that are a factor of 10 – 100 higher than the SFR (the SFR of the fiducial model is shown as the black, dotted curve in the top-left panel). The mass flux builds up quickly in the first 100 Myr and declines gradually thereafter.

The top-right panel shows that the wind velocity peaks at different values at the beginning of the simulations, but converges to similar values after ~ 50 Myr. The peak outflow velocity depends strongly on the temperature increase, with the smallest (largest) value of ~ 400 km s $^{-1}$ (~ 600 km s $^{-1}$) corresponding to the smallest (largest) ΔT . The peak velocity is a measure of the average velocity of gas particles that are able to move freely to large radii. Because our simulations start without a gaseous halo, it is not clear how meaningful the early evolution is, given that the high wind velocities would have resulted in strong shocks if a gaseous halo had been present. However, because the winds fill the haloes with gas, the results quickly become insensitive to the artificial initial conditions. After about 100 Myr the wind velocities of all models converge at about 100 km s $^{-1}$ after which they decline gently to several tens of kilometres per seconds.

The convergence in the SFR, mass outflow rate and

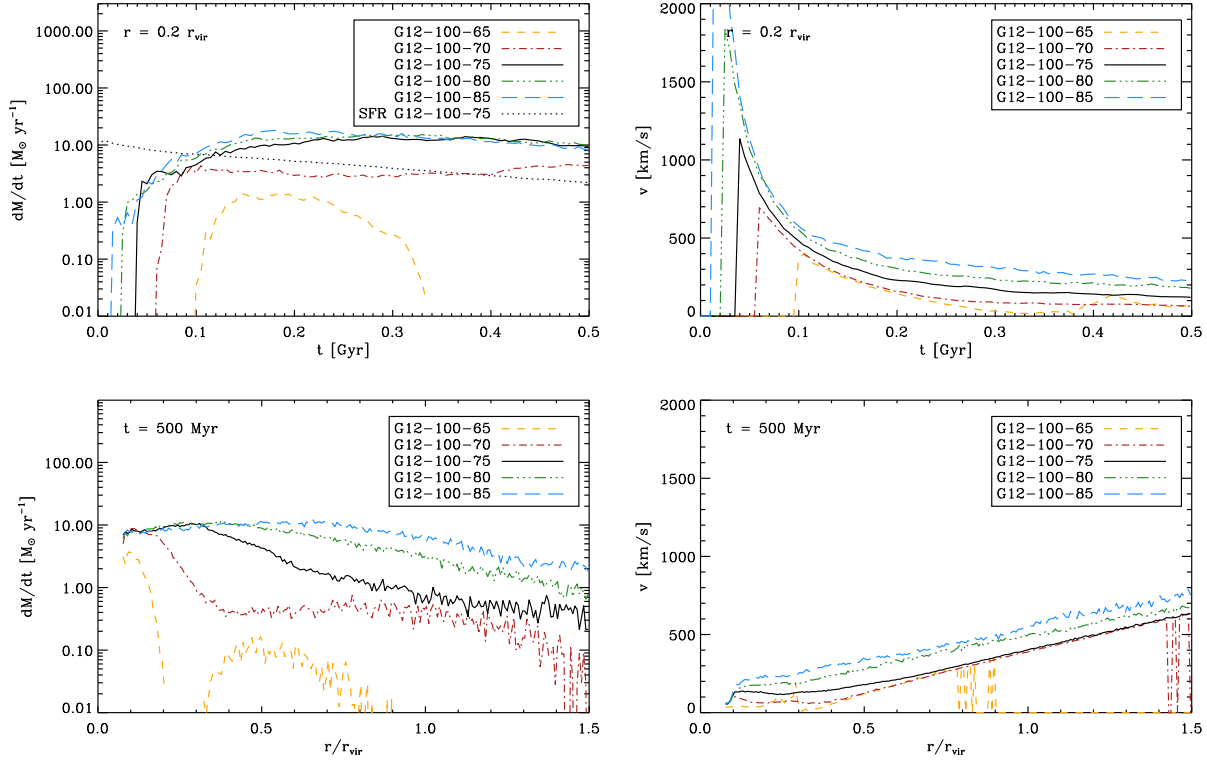


Figure 9. Mass outflow rate (left column) and average outflow velocity (right column) measured through a spherical shell at radius $r = 0.2r_{\text{vir}}$ as a function of time (top row) and at $t = 500$ Myr as a function of radius (bottom row) for models *G12-100-[65,70,75,80,85]*. The dotted line in the top-left panel indicates the SFR of model *G12-100-75*. All other curves are labelled in the legends.

outflow velocity for different values of ΔT indicates that similar amounts of star-forming gas has been extracted from the disc over time. The plots in the bottom row of Fig. 8 confirm that. At each radius the outflow rates and velocities are similar for all models, and the gas can efficiently escape into the halo, and eventually beyond the virial radius.

As was already noted by DS08, the fact that the wind velocity becomes proportional to the radius as we move away from the galaxy (bottom-right panel) is due to travel time effects. Because the wind has only been blowing for a finite amount of time t , only gas with a velocity greater than

$$v = 98 \text{ km s}^{-1} \left(\frac{r}{10 \text{ kpc}} \right) \left(\frac{t}{10^8 \text{ yr}} \right)^{-1}, \quad (26)$$

would be present at radius r if the wind velocity is constant with radius. Although the wind may in reality accelerate or decelerate, our results suggest that travel time effects may well be important too. Hence, wind velocities that are observed to increase with distance do not necessarily imply that the wind is accelerating.

Fig. 9 shows that the picture is different for the massive galaxy. The initial wind velocity is sensitive to the heating temperature and determines the time at which the outflow first passes through the shell at $r = 0.2r_{\text{vir}}$ (corresponding to the sharp rise in the top panels). For $\Delta T \geq 10^{7.5}$ K the mass outflow rates converge at about five times the SFR (the SFR of model *G12-100-75* is indicated by the dotted curve in the top-left panel), so the winds are much less mass-loaded than for the dwarf galaxy. For lower heating temperatures the

mass flux is substantially lower. The outflow rate of model *G12-100-65* even becomes negative after about 320 Myr, indicating net infall (dotted curve in the top-left panel). The wind cannot escape the inner region of the halo, and is confined within a fraction of the virial radius. This model therefore also predicts a much higher SFR (Fig. 7). The fact that the mass flux drops strongly for $\Delta T < 10^{7.5}$ K can be understood by noting that the gas in the central regions and spiral arms has densities $n_{\text{H}} \sim 1 - 10 \text{ cm}^{-3}$ (Fig. 3) and that equation (18) shows that cooling losses should make the feedback inefficient for densities $n_{\text{H}} < 31 \text{ cm}^{-3} (T/10^{7.5})^{3/2}$.

The wind velocities are a factor of a few higher than for the low-mass galaxy and, at least for $\Delta T \geq 10^{7.5}$ K, depend strongly on the temperature increase. Figure 3 showed that for these high heating temperatures, the wind blows channels through which it can freely escape to very large distances. The effect of drag by halo gas is therefore smaller than for the dwarf galaxy and for the low- ΔT versions of the massive galaxy, which all predict much puffier gas disks. Hence, in the high- ΔT simulations of the massive galaxy the outflow speed is predominantly regulated by gravity (as opposed to gas drag) and by the initial velocity. While the potential is always the same, the initial wind velocity is set by the heating temperature.

The radial dependence of the outflow is shown in the bottom row of Fig. 9. Interestingly, the models that predict similar SF histories, also predict similar outflow rates for $r < 0.2r_{\text{vir}}$. However, at larger radii the outflow rates diverge, with higher heating temperatures giving larger mass fluxes.

Except for model *G12-100-65*, the velocities increase linearly with radius beyond about $0.5 r_{\text{vir}}$, suggesting that they are determined by travel time constraints, as was the case for the dwarf galaxy.

6.2 Comparison with the kinetic feedback model

In this section we will compare the results of simulations using our new thermal feedback prescription with runs employing the kinetic feedback of DS08. As discussed in detail in DS08, the kinetic feedback recipe works as follows. Once a star particle reaches an age of 3×10^7 yr, its neighbouring gas particles each have a probability of $\eta m_*/\sum_{i=1}^{N_{\text{ngb}}} m_i$ of receiving a randomly oriented kick of velocity v_w . For the case of equal mass particles, the mass loading factor η equals the average number of particles kicked per star particle. We use DS08's fiducial values of $v_w = 600 \text{ km s}^{-1}$ and $\eta = 2$, which correspond to 40 percent of the available energy.

We compare the kinetic feedback runs to thermal feedback simulations that use the same fraction of the available SN energy (i.e. $f_{\text{th}} = 0.4$ as opposed to 1.0 for our fiducial model). We use a temperature increase of $\Delta T = 10^7 \text{ K}$ (as opposed to $10^{7.5} \text{ K}$ for our fiducial model) as this is close to the post-shock temperature for a shock velocity of 600 km s^{-1} .

To eliminate potential differences other than the feedback recipe, we re-ran models *m12* and *m12nowind* of DS08 with the new code and employing the same softening lengths as used here.

6.2.1 Star formation history

Fig. 10 compares the SF histories of the thermal feedback runs *G10-040-70* and *G12-040-70* with the equivalent kinetic feedback runs *m10* and *m12* of DS08.

We first verify that the new criterion for identifying star-forming gas (see Section 5.1) gives results that are consistent with the implementation used in DS08. In order to eliminate differences due to the feedback implementation, we compare runs without feedback. Comparison of the black and orange dotted curves in Fig. 10, which show the SF histories predicted with the new and old prescriptions, respectively, shows that differences due to the slight change in the recipe for SF are negligible.

Comparing the orange and black solid curves, which show the SF histories in the runs with kinetic and thermal feedback, respectively, we see that the two methods for injecting the energy from SNII are generally in good agreement.

6.2.2 Mass outflow rate and wind velocity

Fig. 11 shows the mass outflow rate (left column) and the mean outflow velocity (right column) for models *G10-040-70* and *m10*. The top row shows the evolution measured at $r = 0.2 r_{\text{vir}}$, while the bottom row illustrates the dependence on radius at time $t = 500 \text{ Myr}$. The agreement is generally excellent. This implies that, at the resolution used for the dwarf galaxy, the average quantities of the outflow are insensitive to the form in which the energy is injected. Note

that this is not a consequence of a fortunate choice of parameters, as we showed in Section 6.1.4 that the outflow is insensitive to the temperature increase ΔT . The agreement between simulations injecting kinetic and thermal energy is consistent with the results of Durier & Dalla Vecchia (2012).

Fig. 12 shows the same plots for the $10^{12} h^{-1} M_{\odot}$ halo. While the agreement for the velocities is again very good, there are in this case some noticeable differences between the mass outflow rates. Compared with the thermal feedback simulation, the kinetic model predicts a higher outflow rate at radii $0.2 \lesssim r/r_{\text{vir}} \lesssim 0.4$ at late times. The differences may imply that the resolution is too low to achieve convergence between kinetic and thermal feedback prescription (recall that the mass resolution is two orders of magnitude lower than for the dwarf galaxy). Another reason, is however, that, unlike for the dwarf galaxy, for the massive galaxy the outflow does depend on the wind parameters. Moreover, for this massive halo $\Delta T = 10^7 \text{ K}$ (or $v_w = 600 \text{ km s}^{-1}$) marks the transition between the regimes of galactic fountains (lower ΔT or v_w) and efficient large-scale winds (higher ΔT or v_w), as can be seen from Figs. 7 and 9. Hence, the results are very sensitive to small differences in the input parameters and we could have obtained better agreement by fine-tuning the value of ΔT (or v_w).

6.3 Resolution tests

We tested the numerical convergence of our implementation of thermal feedback by decreasing the particle numbers by factors of 8 and 64. We will denote the corresponding runs by appending ‘LR008’ resp. ‘LR064’ to the simulation names. Hence, the particle masses are increased by factors of 8 and 64, while the gravitational softening lengths and, for a fixed density, the SPH smoothing kernels are increased by factors of 2 and 4, respectively. Before showing the results, it is useful to consider what we may expect. To do so, we have to check whether the simulations resolve the Jeans scales and whether we expect radiative cooling losses to be significant.

As discussed in Schaye & Dalla Vecchia (2008), for star-forming gas in our fiducial simulation of the massive halo the ratio of the SPH kernel mass to the Jeans mass is smaller than $1/6$ and the ratio of the SPH kernel size to the Jeans length is at most $1/(48)^{1/3} \approx 0.28$. For the low-mass halo the mass and length ratios are lower by factors of 100 and $100^{1/3} \approx 4.64$, respectively. Note that the maximum possible values of these ratios are independent of the density because star-forming particles cannot have temperatures below a power-law effective equation of state with polytropic index $\gamma_{\text{eff}} = 4/3$. Thus, while even our lowest-resolution simulation of the dwarf galaxy resolves the Jeans scales, the same is only true for our highest-resolution simulation of the massive galaxy.

In Section 4 we demonstrated that, for $\Delta T = 10^{7.5} \text{ K}$ and our fiducial resolution for the massive galaxy, radiative losses should have little impact on the efficiency of the feedback if the energy is injected in gas with density $n_{\text{H}} < 31 \text{ cm}^{-3}$ and that this critical density is inversely proportional to the squareroot of the particle mass (eq. [18]). Hence, for the intermediate- and low-resolution models the densities above which radiative losses may prevent efficient feedback are about 11 and 4 cm^{-3} , respectively, and for the low-mass galaxy these densities are 10 times higher. Com-

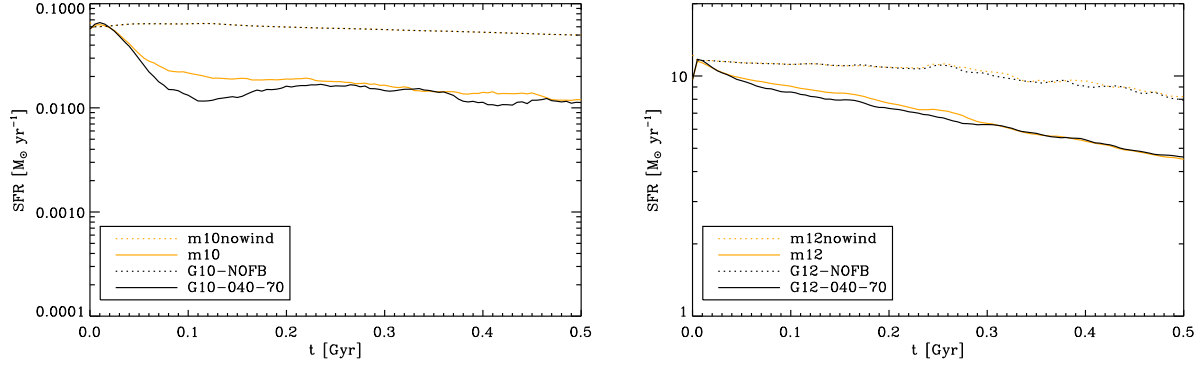


Figure 10. Comparison of the SF histories in simulations employing thermal (*G10-040-70* and *G12-040-70*) and kinetic (*m10* and *m12*) feedback. All models inject 40 percent of the SNII energy. The kinetic feedback assumes an initial wind velocity of 600 km s^{-1} and the thermal feedback a temperature increase of 10^7 K , which is close to the post-shock temperature for a shock velocity of 600 km s^{-1} . The left and right panels show the SFR as a function of time for the 10^{10} and $10^{12} h^{-1} M_{\odot}$ haloes, respectively. The very small difference between the no-feedback models (that are only noticeable for the massive galaxy) are due to the different treatment of star-forming gas (see section 5.1). The two feedback implementations result in very similar SF histories.

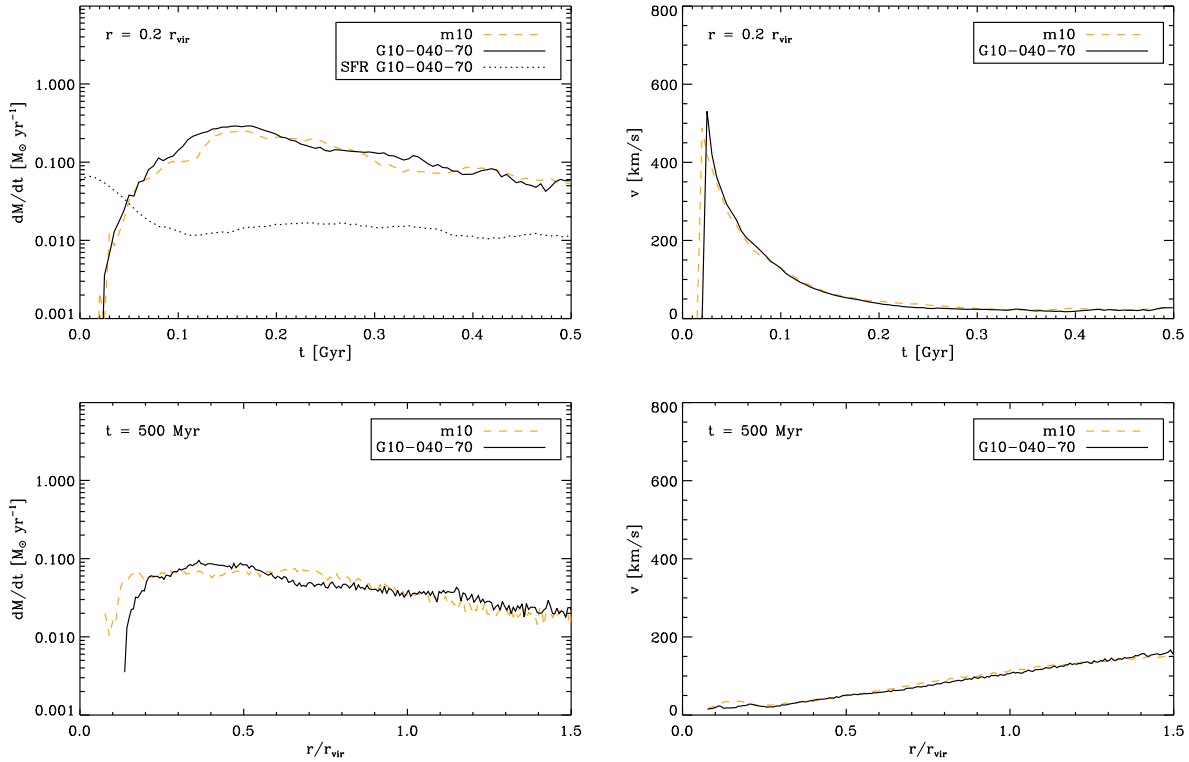


Figure 11. Comparison of the mass outflow rate (left column) and average outflow velocity (right column) measured through a spherical shell at radius $r = 0.2 r_{\text{vir}}$ as a function of time (top row) and at $t = 500 \text{ Myr}$ as a function of radius (bottom row) between model *G10-040-70*, which employs thermal feedback, and model *m10*, which uses kinetic feedback. The dotted curve in the top-left panel indicates the SFR of model *G10-040-70*. All other curves are labelled in the legends. The agreement between the outflows predicted by simulations that inject the SNII energy in thermal and kinetic form is generally excellent.

paring this to the actual densities of the star-forming gas in the high-resolution simulations (Figs. 4 and 5), we see that radiative losses may not be negligible for the lower-resolution simulations of the high-mass galaxy, but that the feedback should remain efficient in the low-resolution models of the dwarf galaxy.

Thus, both Jeans and radiative cooling arguments suggest that even the lowest-resolution simulation of the dwarf galaxy should give converged results. On the other hand, we do expect the lower-resolution versions of the massive galaxy to show some difference. Furthermore, given that the lowest-resolution models have fewer than 3700 gas particles

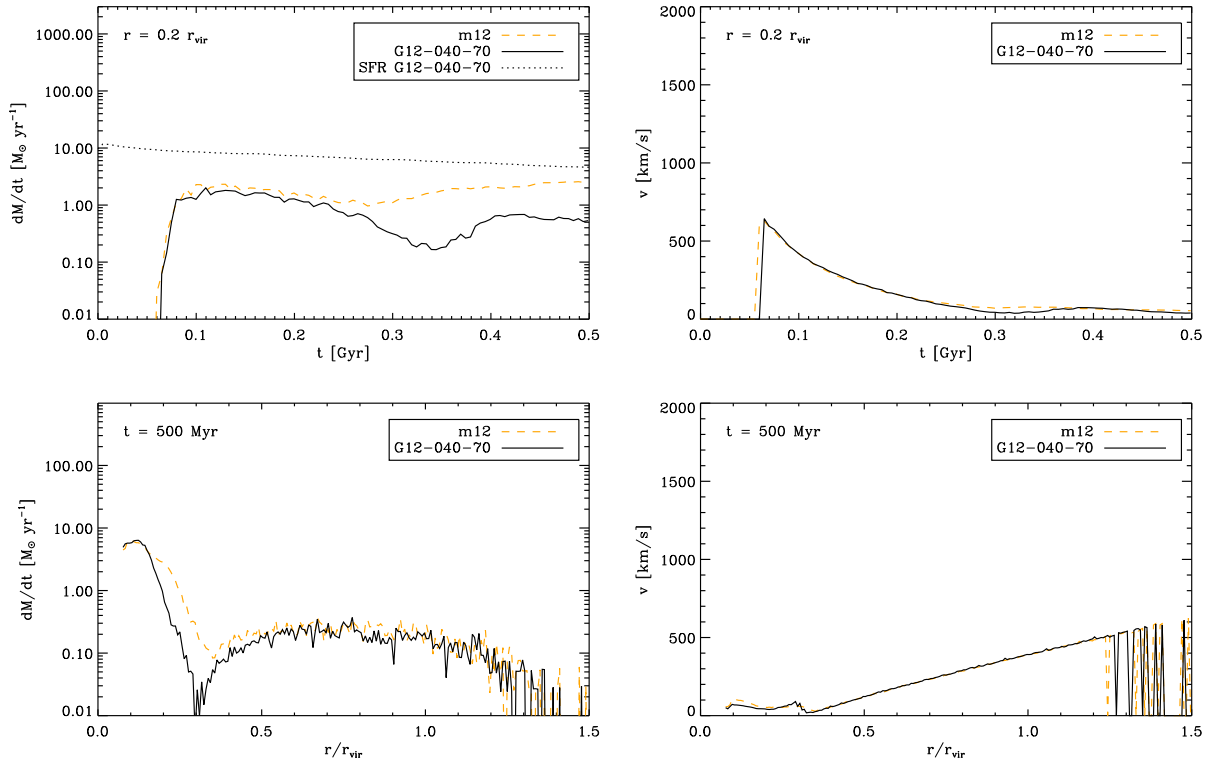


Figure 12. As Fig. 11, but for the $10^{12} h^{-1} M_{\odot}$ halo. The agreement between the thermal and kinetic implementations of SNII feedback is very good for the wind velocities, but the mass outflow rates differ substantially at late times and intermediate radii. This probably reflects the fact that these wind parameter values yield results that are intermediate between the galactic fountain and efficient, large-scale winds regimes, making the outcome very sensitive to the exact values of the wind parameters.

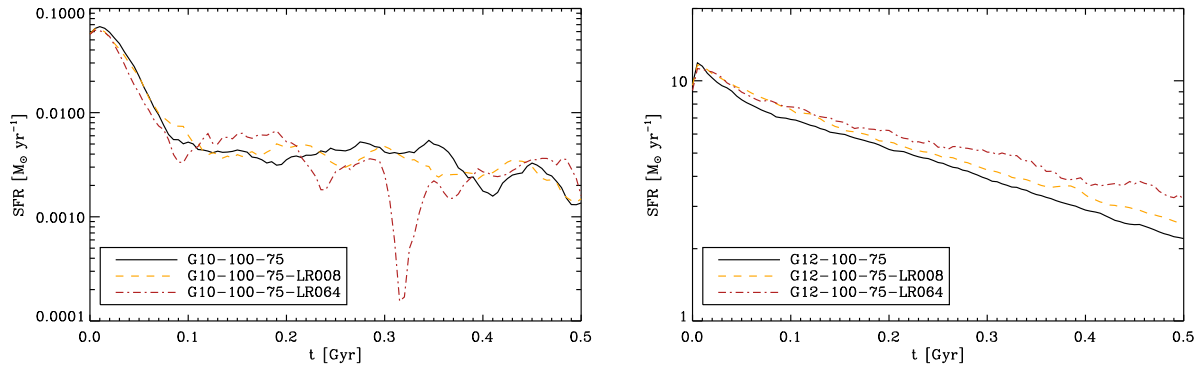


Figure 13. Numerical convergence of the SF histories of the $10^{10} h^{-1} M_{\odot}$ and $10^{12} h^{-1} M_{\odot}$ haloes (left- and right panels, respectively). The mass resolution is decreased by factors of 8 (dashed curves) and 64 (dash-dotted curves). The convergence is good, although there is a small, systematic increase of the SFR with decreasing resolution for the massive galaxy.

in the disk, we expect the results to become noisy due to the poor sampling.

Figs. 13 shows how the SF history depends on the numerical resolution for the fiducial models *G10-100-75* (left) and *G12-100-75* (right). Similarly, Fig. 14 illustrates the resolution dependence of the predicted evolution of the mass outflow rate (left column) and wind velocity (right column) for the dwarf (top row) and massive (bottom row) galaxies. Clearly, our expectations are borne out.

Whereas the dwarf galaxy runs are very well converged,

for the massive galaxy the predicted SFR increases with resolution, although the effect is small. The first 250 Myr the mass outflow rate is somewhat higher in the lower resolution simulations of the massive galaxy, but the situation reverses at later times. Except for the first 10 Myr, the differences are, however, small. The wind velocity is more sensitive to the resolution and is generally higher in the lower-resolution models. The predictions for the outflow properties become noisy for the lowest resolution simulations.

It is interesting that the convergence with numerical

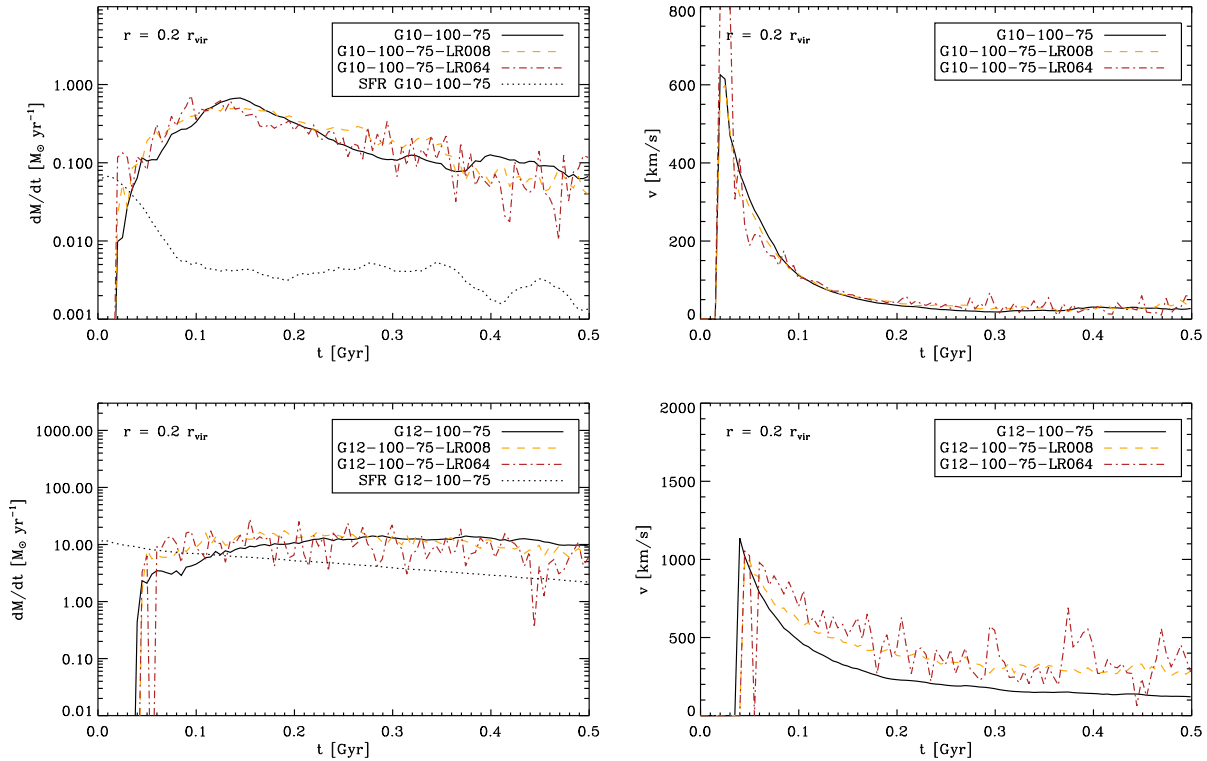


Figure 14. Resolution dependence of the mass outflow rate (left column) and mean outflow velocity (right column) measured through a spherical shell at radius $r = 0.2 r_{\text{vir}}$ as a function of time for the 10^{10} (top row) and the $10^{12} h^{-1} M_{\odot}$ (bottom row) haloes. Note that the particle mass in *G10-100-75-LR064* is still lower than that in *G12-100-75*. While the predictions for the low-mass galaxy are converged, decreasing the resolution yields mostly higher outflow velocities for the high-mass galaxy, but has little effect on the mass outflow rates.

resolution is better than found by DS08 for the kinetic feedback versions of the same simulations (c.f. Figs. 10 and 11 of DS08). For example, with kinetic feedback the outflow rate for the massive galaxy increased by a factor of about 3 as the mass resolution was decreased by a factor of 8 and the SFR of the dwarf galaxy increased substantially when the particle mass was decreased by a factor of 64. It should be kept in mind, however, that this could in part be due to the fact that the fiducial wind velocity used by DS08 (600 km s^{-1}) corresponds to post-shock temperature jumps that are a factor of a few lower than our fiducial value of $\Delta T = 10^{7.5} \text{ K}$.

7 DISCUSSION

Models of galaxy formation and evolution require feedback from star formation to reproduce the observed properties of galaxies. Cosmological simulations do not have sufficient resolution to resolve individual SN explosions and must therefore resort to sub-grid recipes. The simplest method, injecting the SN energy released by a star particle (i.e. a simple stellar population; SSP) during each time step into its surroundings, does not lead to efficient feedback because the injected thermal energy is quickly radiated away. Successful recipes generally either inject the energy in kinetic form, turn off radiative cooling temporarily, or inject the energy in a hot sub-grid phase that is decoupled from the colder phases by hand.

We demonstrated that the catastrophic radiative losses suffered by simple thermal feedback recipes are due to a mismatch between the gas mass in which the energy is injected and the mass of the SSP that produced the energy. In the real Universe, one SNII is produced for every $\sim 10^2 M_{\odot}$ of stars, and the energy released in the explosion is initially carried by $\ll 10^2 M_{\odot}$ of ejecta. Because the ratio between the mass of the ejecta and the mass of the stellar population that released the energy is small ($\ll 1$), the SN energy per unit mass of ejecta is high. Hence, the ejecta move at very high velocity ($\gg 10^3 \text{ km s}^{-1}$) and the post-shock temperatures are sufficiently large for the radiative cooling time to be long. Indeed, observations do provide evidence for hot gas associated with fast galactic outflows (e.g. Heckman, Armus, & Miley 1987; Strickland et al. 2000; see also the review by Veilleux, Cecil, & Bland-Hawthorn 2005).

In simulations, however, the ratio between the gas mass receiving the SN energy and the stellar mass that produced it is much larger. Even if all the SNII energy of an SSP is injected at once, the ratio between the mass of the ‘ejecta’ and that of the SSP will typically be large. For example, if, for the case of SPH, the energy is shared by all N_{SPH} neighbours, then the ratio will be $N_{\text{SPH}} \gg 10$ and even larger if multiple star particles are spawned per gas particle or if the feedback energy is released over multiple time steps. Consequently, the temperature of the heated particles will be relatively low and most of the thermal energy will

be radiated away before it is able to do PdV work on its surroundings. It is important to note that the ratio between the gas mass receiving the energy and the mass of the SSP that produced it is independent of the resolution.

The realisation that the cause of the inefficient thermal feedback is a mismatch between the simulated and observed ratios of heated mass to stellar mass, rather than a straightforward lack of numerical resolution, immediately indicates the solution: we need to decrease this ratio in the simulations. By decreasing the mass ratio, we increase the temperature of the heated gas and hence its cooling time. If the cooling time is long compared with the sound crossing time scale across a resolution element, the heated gas will begin to expand adiabatically and the injected thermal energy will be efficiently converted into kinetic energy. We showed that in the temperature regime for which Brehmsstrahlung dominates the radiative cooling rate ($\gtrsim 10^7$ K for solar abundances), the ratio of the cooling time and the sound crossing time remains constant if the gas expands adiabatically, so that adiabatic cooling does not invalidate the argument.

We showed analytically (see eq. [18]) that, for the case of SPH, the maximum density for which radiative losses are small is $n_H \sim 26 \text{ cm}^{-3} (T/10^{7.5} \text{ K})^{3/2} (m/10^5 \text{ M}_\odot)^{-1/2}$, where T is the temperature of the heated gas after receiving the feedback energy and m is the mass of a gas resolution element (and we assumed that ΔT is sufficiently high for Brehmsstrahlung to dominate the radiative cooling). The maximum density is nearly the same for AMR simulations with cell sizes that are at least a factor of 4 smaller than the local Jeans length (evaluated in gas with this density and a temperature of 10^4 K, see eq. [20]). Hence, by specifying the desired temperature jump ΔT , we can guarantee that the feedback is efficient up to some gas density that we can estimate analytically.

We implemented this idea in the SPH code *GADGET* in the form of stochastic thermal feedback. A fixed ΔT then translates into a fixed probability of receiving energy, which we evaluate for each SPH neighbour of a star particle that has just crossed the critical age $t_{\text{SN}} = 3 \times 10^7$ yr, corresponding to the maximum lifetime of stars that end their lives as SNII. For a Chabrier IMF and assuming equal mass particles, the expectation value of the number of heated particles is $1.34 f_{\text{th}} (\Delta T/10^{7.5} \text{ K})^{-1}$, where f_{th} is the fraction of the SNII energy that is injected (see eq. [8]).

Note that the parameter ΔT plays a similar role as the initial wind velocity v_w for the case of kinetic feedback. For a fixed v_w , the mass loading factor used in kinetic feedback implementations sets f_{th} . The fraction of the injected SN energy can also be used as a second free parameter for the case of thermal feedback. For a fixed temperature jump, the “initial mass loading” is then the ratio of the heated mass per unit stellar mass formed and this ratio is proportional to the parameter f_{th} .

The combination of stochastic feedback and a fixed increase in the energy per unit mass of the gas receiving the feedback energy also works for kinetic feedback: we can specify v_w and give each neighbouring resolution element of a star particle a probability of being kicked in the wind that is proportional to the mass loading factor or, equivalently, to f_{th} . This is in fact exactly the implementation of kinetic feedback that we used in DS08.

The equivalence of the roles of ΔT and v_w suggests

that the efficiency of the kinetic feedback does not depend directly on the ratio of the initial wind velocity and the escape velocity, contrary to what is often assumed. Indeed, in DS08 we showed that if v_w is too low, the wind stalls in the ISM, before it has even begun to climb out of the gravitational potential. As we have shown, the efficiency of the wind depends on the radiative losses and hence, for a fixed value of v_w , on the numerical resolution and the gas density. Because the typical gas densities increase with the gas pressure and thus with the depth of the potential well, the escape velocity does matter indirectly (also because drag forces increase with the pressure). If the wind manages to blow out of the ISM, then the ultimate efficiency of the feedback does depend on the ratio of the velocity of the wind leaving the ISM and the escape velocity, because the ejected gas will rain back onto the galaxy if it cannot escape the galaxy’s potential well.

We presented analytic derivations of the resolution criteria, both for SPH and AMR simulations. We tested our recipe for thermal feedback on SPH simulations of isolated disc galaxies in dark matter haloes of total mass $10h^{-1} \text{ M}_\odot$ and $10^{12}h^{-1} \text{ M}_\odot$ using the same set-up as we used to study kinetic SN feedback in DS08. We explored the effect of the feedback on the gas distribution, the star formation history, the mass outflow rate, and the wind velocity. The results were in accord with our analytic predictions.

For sufficiently high ΔT and for sufficiently high resolution, the thermal feedback strongly reduces the star formation rate and results in a strong, large-scale, bi-polar outflow. Reassuringly, the results converge with both ΔT and resolution and the converged results also agree well with simulations employing kinetic feedback⁵ (with sufficiently high v_w).

However, if ΔT and/or the resolution are too low, then the results become sensitive to both. For a fixed resolution, higher values of ΔT will then result in more efficient feedback. Hence, in this regime the ability to choose ΔT or, for the case of kinetic feedback v_w , implies a considerable freedom. This freedom associated with the implementation of feedback from star formation is currently the limiting factor for the predictive power of cosmological simulations (e.g. Schaye et al. 2010; Scannapieco et al. 2011).

Given that a higher ΔT yields smaller radiative losses, one may ask why we do not use ultra-high values. Indeed, even in low-resolution simulations the feedback could be made efficient locally by increasing ΔT (or v_w for the case of kinetic feedback). There are, however, several reasons why it is undesirable to increase this parameter to values $> 10^8$ K. First, even for $f_{\text{th}} = 1$ such high heating temperatures imply that, on average, each star particle will heat less than one neighbouring gas particle. Such a situation breaks the locality of the feedback and may lead to sampling problems. That this can have grave consequences is easy to see by considering the limiting case in which the number of heated gas particles per star particle (i.e. the mean initial mass loading) is $\ll 1$. Most heavy elements released by massive stars will

⁵ The thermal feedback models only agree with kinetic feedback simulations if the kicked wind particles are *not* temporarily decoupled from the hydrodynamics, see DS08 for a critical discussion of this common practice.

then no longer be injected in a wind. Many generations of star particles can form in a given gas cloud before a single feedback event takes place. Conversely, if, despite the low probability, a star particle forming in a region with a low star formation density does heat a neighbour, the energy injected may be sufficiently large to do catastrophic damage. Clearly, we should avoid the regime in which the expectation value for the number of heated gas elements per star particle formed is much less than one, at least for galaxies resolved with relatively small numbers of particles.

At present, large-volume cosmological simulations typically have particle masses $\gtrsim 10^6 M_\odot$. At this resolution even heating one gas particle per star particle (which corresponds to $\Delta T \sim 10^{7.5}$ K for a Chabrier IMF and $f_{\text{th}} = 1$) results in strong radiative losses for densities $n_{\text{H}} > 10 \text{ cm}^{-3}$, which are routinely reached in such simulations. Hence, the predictions are still sensitive to the values of the feedback prescription and are thus uncertain. This undesirable limitation can be turned into an advantage if one takes an approach similar in spirit to semi-analytic models: by varying ΔT (or v_{w}) with halo mass or with the local physical conditions, the feedback can be tuned to reproduce the desired galaxy formation efficiency. However, the arguments given above demonstrate that the results may change with increasing resolution⁶. If the resolution and the value of ΔT are sufficiently high for cooling losses to be small, then the feedback can still be tuned by varying f_{th} with the local conditions.

We have demonstrated that, contrary to common wisdom, thermal feedback can be efficient without turning off radiative cooling. For sensible parameter choices overcooling can already be avoided for densities typical of the warm ISM (i.e. $n_{\text{H}} \sim 1 \text{ cm}^{-3}$) at the resolution achievable for large-scale cosmological simulations ($m \sim 10^7 M_\odot$) and for simulations of individual (low- to intermediate-mass) galaxies we can already afford the resolution ($m \sim 10^2 M_\odot$) required for the feedback to remain efficient up to densities typical of molecular clouds ($n_{\text{H}} \sim 10^3 \text{ cm}^{-3}$). We have also shown that with sufficient resolution, the results become insensitive to the problematic parameter of the feedback implementation (i.e. ΔT for thermal feedback and v_{w} for kinetic feedback) and the form in which the energy is injected, thus removing some of the most important uncertainties in the ingredients of hydrodynamical simulations of galaxy formation.

ACKNOWLEDGEMENTS

We are very grateful to Volker Springel for allowing us to use GADGET and his initial conditions code for the simulations presented here. We thank Rob Crain and Jarrett Johnson for a careful reading of the manuscript, and the anonymous referee for a helpful report. The simulations presented here were run on the Cosmology Machine at the Institute for Computational Cosmology in Durham as part of the Virgo Consortium research programme and on the TMOx cluster

at the Rechenzentrum Garching of the Max Planck Society. This work was supported by Marie Curie Reintegration Grant FP7-RG-256573 and by the Marie Curie Initial Training Network CosmoComp (PITN-GA-2009-238356).

REFERENCES

- Booth C. M., Schaye J., 2009, MNRAS, 398, 53
- Brook C. B., Kawata D., Gibson B. K., Flynn C., 2004, MNRAS, 349, 52
- Chiosi C., Bertelli G., Bressan A., 1992, ARA&A, 30, 235
- Creasey P., Theuns T., Bower R. G., Lacey C. G., 2011, MNRAS, 415, 3706
- Dalla Vecchia C., Schaye J., 2008, MNRAS, 387, 1431 (DS08)
- Dubois Y., Teyssier R., 2008, A&A, 477, 79
- Durier F., Dalla Vecchia C., 2012, MNRAS, 419, 465
- Ferland, G. J. 2000, Revista Mexicana de Astronomia y Astrofisica Conference Series, 9, 153
- Gerritsen J. P. E., 1997, PhD
- Haardt, F., & Madau, P. 2001, in the proceedings of XXXVI Rencontres de Moriond, astro-ph/0106018
- Heckman T. M., Armus L., Miley G. K., 1987, AJ, 93, 276
- Hopkins P. F., Quataert E., Murray N., 2012, MNRAS, 421, 3522
- Kawata D., 2001, ApJ, 558, 598
- Katz N., Weinberg D. H., Hernquist L., 1996, ApJS, 105, 19
- Kay S. T., Pearce F. R., Frenk C. S., Jenkins A., 2002, MNRAS, 330, 113
- Kay S. T., Thomas P. A., Theuns T., 2003, MNRAS, 343, 608
- Kennicutt R. C., Jr., 1998, ApJ, 498, 541
- Marri S., White S. D. M., 2003, MNRAS, 345, 561
- Mihos J. C., Hernquist L., 1994, ApJ, 437, 611
- Monaghan J. J., 1997, JCoPh, 136, 298
- Mori M., Yoshii Y., Tsujimoto T., Nomoto K., 1997, ApJ, 478, L21
- Murante G., Monaco P., Giovalli M., Borgani S., Diaferio A., 2010, MNRAS, 405, 1491
- Navarro J. F., White S. D. M., 1993, MNRAS, 265, 271
- Oppenheimer B. D., Davé R., 2006, MNRAS, 373, 1265
- Osterbrock D. E., 1989, *agnabook*,
- Piontek F., Steinmetz M., 2011, MNRAS, 410, 2625
- Saitoh T. R., Makino J., 2009, ApJ, 697, L99
- Scannapieco C., Tissera P. B., White S. D. M., Springel V., 2006, MNRAS, 371, 1125
- Scannapieco C., Wadepuhl M., Parry O. H., et al., 2011, arXiv:1112.0315
- Schaye J., 2004, ApJ, 609, 667
- Schaye J., Dalla Vecchia C., 2008, MNRAS, 383, 1210
- Schaye J., Dalla Vecchia C., Booth C. M., et al., 2010, MNRAS, 402, 1536
- Sommer-Larsen J., Götz M., Portinari L., 2003, ApJ, 596, 47
- Springel V., Hernquist L., 2003, MNRAS, 339, 289 (SH03)
- Springel V., 2005, MNRAS, 364, 1105
- Springel V., Di Matteo T., Hernquist L., 2005, MNRAS, 361, 776
- Stinson G., Seth A., Katz N., Wadsley J., Governato F., Quinn T., 2006, MNRAS, 373, 1074

⁶ Turning off the hydrodynamical forces in the high-density regime could make the results insensitive to resolution for kinetic feedback (Springel & Hernquist 2003), but the predictions will in that case disagree with converged, self-consistent high-resolution simulations.

- Strickland D. K., Heckman T. M., Weaver K. A., Dahlem M., 2000, *AJ*, 120, 2965
- Thacker R. J., Couchman H. M. P., 2000, *ApJ*, 545, 728
- Theuns T., Leonard A., Efstathiou G., Pearce F. R., Thomas P. A., 1998, *MNRAS*, 301, 478
- Veilleux S., Cecil G., Bland-Hawthorn J., 2005, *ARA&A*, 43, 769
- Wiersma R. P. C., Schaye J., Smith B. D., 2009a, *MNRAS*, 393, 99
- Wiersma R. P. C., Schaye J., Theuns T., Dalla Vecchia C., Tornatore L., 2009b, *MNRAS*, 399, 574